Magnetar giant flare high-energy emission

Elenbaas, C.; Huppenkothen, D.; Omand, C.; Watts, A.L.; Bissaldi, E.; Caiazzo, I.; Heyl, J.

DOI
10.1093/mnras/stx1727

Publication date
2017

Document Version
Final published version

Published in
Monthly Notices of the Royal Astronomical Society

Monthly Notices
of the
ROYAL ASTRONOMICAL SOCIETY

MNRAS **471,** 1856–1872 (2017)
Advance Access publication 2017 July 13

doi:10.1093/mnras/stx1727

Magnetar giant flare high-energy emission

C. Elenbaas,[1]★ D. Huppenkothen,[2,3] C. Omand,[4,5] A. L. Watts,[1] E. Bissaldi,[6,7] I. Caiazzo[4] and J. Heyl[4]

[1]*Anton Pannekoek Institute for Astronomy, University of Amsterdam, Science Park 904, NL-1098 XH Amsterdam, the Netherlands*
[2]*Center for Cosmology and Particle Physics, Department of Physics, New York University, 4 Washington Place, New York, NY 10003, USA*
[3]*Center for Data Science, New York University, 65 5th Avenue, 7th Floor, New York, NY 10003, USA*
[4]*Department of Physics and Astronomy, University of British Columbia, 6224 Agricultural Road, Vancouver, BC V6T 1Z1, Canada*
[5]*Department of Physics, Graduate School of Science, The University of Tokyo, 7-3-1 Hongo, Bunkyo-ku, Tokyo 113-8656, Japan*
[6]*Dipartimento Interateneo di Fisica, Politecnico di Bari, Via E.Orabona 4, 70125 Bari, Italy*
[7]*INFN – Sezione di Bari, Via E.Orabona 4, I-70125 Bari, Italy*

Accepted 2017 July 6. Received 2017 July 6; in original form 2017 March 31

ABSTRACT

High-energy (>250 keV) emission has been detected persisting for several tens of seconds after the initial spike of magnetar giant flares (GFs). It has been conjectured that this emission might arise via inverse Compton scattering in a highly extended corona generated by super-Eddington outflows high up in the magnetosphere. In this paper, we undertake a detailed examination of this model. We investigate the properties of the required scatterers, and whether the mechanism is consistent with the degree of pulsed emission observed in the tail of the GF. We conclude that the mechanism is consistent with current data, although the origin of the scattering population remains an open question. We propose an alternative picture in which the emission is closer to that star and is dominated by synchrotron radiation. The *Reuven Ramaty High Energy Solar Spectroscopic Imager* observations of the 2004 December flare modestly favour this latter picture. We assess the prospects for the *Fermi Gamma-ray Space Telescope* to detect and characterize a similar high-energy component in a future GF. Such a detection should help to resolve some of the outstanding issues.

Key words: magnetic fields – radiation mechanisms: non-thermal – scattering – stars: magnetars.

1 INTRODUCTION

Magnetars are neutron stars (NSs) with magnetic fields at the extreme high end of the distribution, in the range 10^{13}–10^{15} G. One of their defining characteristics, indeed the one that led to their discovery (Mazets et al. 1979; Mazets & Golenetskii 1981), is the repeated emission of bursts of hard X-rays and γ-rays. The bursts are assumed to be powered by magnetic field decay (Thompson & Duncan 1995), yet many details of the burst trigger and emission process remain unsolved (see Turolla, Zane & Watts 2015, for a recent review).

Bursts come in a range of fluences, but the brightest are the rare giant flares (GFs) with energies in the range 10^{44}–10^{46} erg (if the emission is isotropic). Only three have been observed over the last 38 yr, each from a different magnetar. Their properties are very similar: a very bright initial spike lasting ∼0.1–1 s followed by a decaying tail lasting several hundred seconds, strongly pulsed at the few second spin period of the star (Mazets et al. 1979; Hurley et al. 1999, 2005).

The initial γ-ray spike is very hard, with emission being detected up to a few MeV (Mazets et al. 1979; Hurley et al. 1999). It is thought to originate in particle acceleration as the evolving magnetic field reaches a tipping point and undergoes explosive reconfiguration or reconnection. Rapid acceleration of electrons in a strong curved magnetic field leads naturally to a cascade of γ-rays and pair creation (Sturrock, Harding & Daugherty 1989). The existence of radio afterglows points to the simultaneous ejection of a plasmoid of relativistic particles and magnetic fields that then energizes a pre-existing shell of surrounding material (Frail, Kulkarni & Bloom 1999; Cameron et al. 2005; Granot et al. 2006).

Many of the electron–positron pairs from the initial event become trapped in closed field regions, with optical thickness high enough to trap the photons, leading to rapid thermalization (Thompson & Duncan 1995). This hot pair-plasma fireball cools and contracts relatively slowly, generating the long tail. The emission is strongly beamed by super-Eddington mildly relativistic outflows driven by the radiation escaping from the fireball (Thompson & Duncan 1995, 2001; van Putten et al. 2013, 2016). Although the

★ E-mail: cpc.elenbaas@gmail.com

temperature in the core of the fireball is thought to be ∼100 keV, the emerging radiation has a photospheric temperature ∼10–30 keV.

Following the GF from the magnetar SGR 1806−20 in 2004 December, Boggs et al. (2007) reported the detection of two hard non-thermal components in the spectrum after the initial spike. One power-law (PL) component extends up to $\gtrsim$250 keV and persists throughout the pulsed tail. However, there is also a second PL component that extends up to 17 MeV (the limit of the *Reuven Ramaty High Energy Solar Spectroscopic Imager, RHESSI* instrument) with no sign of a cut-off. Frederiks et al. (2007) also report the observation of a high-energy PL component extending up to the sensitivity limit of the Konus–Wind detector, i.e. 10 MeV. A hard tail (∼300–650 keV) was observed by Feroci et al. (1999) for the 1998 August 27 GF of SGR 1900+14, where the upper limit was constrained by the sensitivity of the *Gamma-Ray Burst Monitor* (*GBM*) on board the *BeppoSAX* spacecraft.

The non-thermal component at the lower end of the energy spectrum is thought to emerge from electron cyclotron scattering in an extended corona (∼5–10 $R_{\rm NS}$, where $R_{\rm NS}$ is the radius of the NS), where output photon energies in excess of 100 keV are attainable (Thompson, Lyutikov & Kulkarni 2002; Boggs et al. 2007). The hard energy component that reaches tens of MeV however is conjectured by Feroci et al. (2001) and Boggs et al. (2007) to originate in a *highly* extended corona, generated by super-Eddington outflows, high up in the magnetosphere (∼100 $R_{\rm NS}$). At these altitudes, the magnetic energy density has become less than the energy density of the X-ray emission, i.e. $u_{\rm B} < u_{\rm X}$, and the charges cool through inverse Compton (IC) scattering, rather than synchrotron emission. The hard non-thermal tail is thus argued to be the result of IC scattering of the emission on to the charges that make up this additional extended corona.[1]

Note that during quiescence, a non-thermal PL component is also observed in the hard X-ray range (>20 keV) of various magnetars: 4U 0142+614, 1RXS J1708−4009, 1E 1841−045, 1E 2259+586, SGR 1806−20, and SGR 1900+14 (Kuiper, Hermsen & Mendez 2004; Kuiper et al. 2006; Mereghetti et al. 2005; Molkov et al. 2005; Götz et al. 2006; Enoto et al. 2011; Turolla et al. 2015). The non-detection of γ-ray emission by Comptel and *Fermi Large Area Telescope (LAT)* from quiescent magnetars, suggest a spectral cut-off of this component at ∼few hundred keV (den Hartog et al. 2006; Kuiper et al. 2006; Şaşmaz Muş & Göğüş 2010). Various mechanisms have been invoked to explain the hard quiescent emission. Thompson & Beloborodov (2005) consider two scenarios: (i) thermal Bremsstrahlung through crustal heating by return currents and (ii) synchrotron radiation (peaking at ∼1.5 MeV) from energetic pairs created by Comptonized X-ray photons on accelerated positrons in the magnetosphere (at ∼10 $R_{\rm NS}$). Another possibility is resonant cyclotron scattering (RCS) of a thermal seed photon population (Baring, Gonthier & Harding 2005; Baring & Harding 2007). This scenario has been studied in detail with relativistic full QED 3D Monte Carlo codes that model the hard component (Nobili, Turolla & Zane 2008a,b; Zane et al. 2011).

[1] The smooth ∼40 s decay that followed the initial spike of the GF from SGR 1900+14 on 1998 August 27, is argued to have been the signature of a pair corona, produced by post burst onset seismic activity, that surrounded the fireball (∼10 $R_{\rm NS}$) and gradually evaporated (Thompson & Duncan 2001; Feroci et al. 2001). This corona proceeded to Compton scatter O-mode photons seeping out at the base of the fireball hardening the emergent emission. Note however that this corona is dissimilar from the highly extended corona (∼100 $R_{\rm NS}$), invoked to explain the second hard component (∼0.4–17 MeV), that upscatters photons at the outer edges of the X-ray jets.

The latter are limited by their use of a self-similar twisted magnetic dipole and simple charge velocity distribution. Phase-resolved spectroscopy of Anomalous X-ray pulsars (AXPs) 1RXS 4U 0142+61 and J1708−4009 suggest however the presence of more complex magnetic field configurations (den Hartog et al. 2008a; den Hartog, Kuiper & Hermsen 2008b). The effects of higher multipolar and locally twisted configurations on the emergent high-energy spectra were investigated by Pavan et al. (2009) and Viganò et al. (2012), respectively. Beloborodov (2012) explored the emergent spectrum from a more physically motivated model for the charge velocity distribution on a locally twisted magnetic bundle.

In quiescence, the non-thermal flux is typically $\sim 10^{-12}$ erg cm^{-2} s^{-1}, and the cooling time for RCS is 0.1 ms, about a light-crossing time. During the burst, the non-thermal flux above 1 MeV is 10^6 times larger, and the non-thermal flux continues nearly ∼100 s. So although the RCS mechanism could account for the instantaneous high-energy spectrum during the burst, the energy content of the quiescent population of high-energy electrons falls short by 12 orders of magnitude.

The purpose of this paper is to examine in detail the mechanism that could generate the highest energy MeV emission, particularly IC scattering in an extended pair corona high up in the magnetosphere. We consider the properties of the scatterers that would be required to generate the highest energy emission. We contrast these results with those from a model where synchrotron emission dominates the high-energy radiation. We also consider whether these mechanisms are consistent with the observed high-energy spectrum and the degree to which the emission during the tail is pulsed. Determining amplitudes and upper limits on periodic signals during magnetar bursts is complicated by the fact that the signal has a strong red noise component, as well as the changes in source brightness relative to the sky background imposed by the spectral dependence. We build a Bayesian model to take both effects into account in our analysis.

We also examine the prospects for future detection of high-energy components during GFs. The facility that is best suited to do this is NASA's *Fermi Gamma-ray Space Telescope* (*FGST* or *Fermi*) that has been operational since 2008 and will be until at least 2018. *Fermi* has two instruments: the *GBM*, which provides near full coverage of the unocculted sky in the ∼0.01–38 MeV energy band (Meegan et al. 2009) and has been a very prolific burst detector (Collazzi et al. 2015; Bhat et al. 2016); and the *LAT* provides high-energy coverage with a field of view (FoV) ∼2.4 sr in the ∼80–10^4 MeV energy band (Atwood et al. 2009). The latter has been used to study the γ-ray upper limits on magnetars (Abdo et al. 2010; Li et al. 2016).

2 OBSERVATIONS AND ANALYSIS

2.1 Giant flare high-energy emission

The *RHESSI* is a solar telescope dedicated to the exploration of energetic transient phenomena, such as explosive particle acceleration during solar flares, over a broad energy bandpass (3 keV–17 MeV) and at a native time resolution of 1 binary μs (2^{-20} s $\simeq 9.5 \times 10^{-7}$ s). The principal instrument comprises an array of nine coaxial high-purity germanium detectors (each with 1 front and 2 rear segments; the former records X-rays up to ∼100 keV and the latter detect photons with energies $\gtrsim$100 keV), which are unshielded and may record photons from off-axis sources (Smith et al. 2002). *RHESSI* employs mobile attenuators to inhibit incoming flux from high intensity flares as to prevent saturation due to excessive count rates;

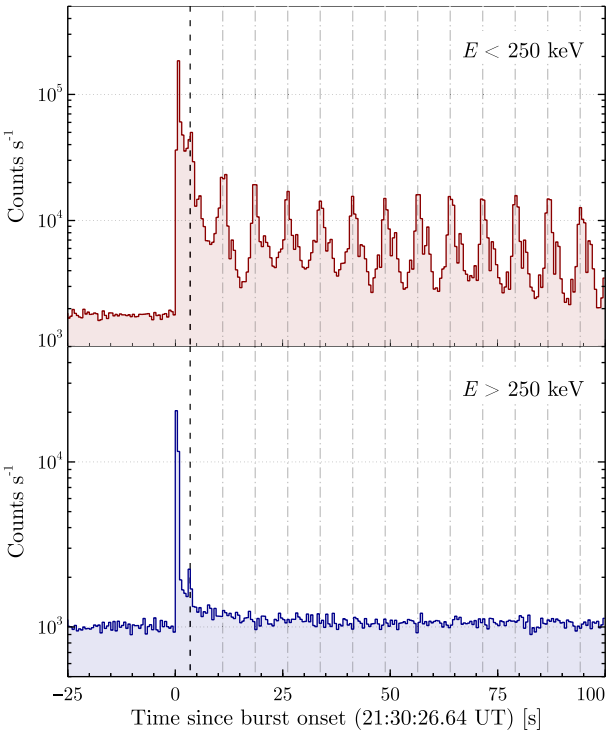

Figure 1. Count rate versus time of the *RHESSI* detectors. The GF starts at $t_0 = 21{:}30{:}26.64$ UT. The upper (lower) plot displays the low (high) energy count rate, i.e. counts with a recorded energy <250 keV (>250 keV). The initial hard spike lasts ∼0.2 s and is followed by a soft tail with a series of superimposed pulsations at the spin period of the NS, i.e. $P_{\rm NS} \simeq 7.56$ s (Woods et al. 2007). The first pulse occurs at $t - t_0 \sim 3.47$ s, denoted by the vertical dashed line and coincides with an instrumental artefact – see Appendix C. The subsequent pulse maxima are denoted by the vertical dash–dotted lines. The pulsations are not apparent in the high-energy emission. The plot is truncated at $t - t_0 = 100$ s. Recorded counts of all detector segments (front and rear) where used in these plots.

their motion however can lead to significant instrumental artefacts in the data (see Appendix C).

On 2004 December 27 at $t_0 = 21{:}30{:}26.64$ UT, *RHESSI* recorded a GF a mere ∼5° off-axis, that originated from the magnetar SGR 1806–20 (see Fig. 1); the third and most energetic magnetar GF ever observed, with total energy (assuming isotropic emission) $\sim 10^{46}$ erg (Hurley et al. 2005). A detailed analysis of the obtained *RHESSI* data was presented by Boggs et al. (2007). In particular, they demonstrated the presence of a non-thermal high-energy emission component (>400 keV) following the onset of the flare that lasts a few tens of seconds. In this section, we first reproduce their results regarding the high-energy emission, and then further investigate the temporal and spectral properties of the event.

2.2 Temporal and spectral properties

We begin by repeating the analysis performed by Boggs et al. (2007) to confirm the general properties of the high-energy component. The presence of the high-energy excess emission (0.4–10 MeV) is demonstrated in Fig. 2, where the counts, recorded in the rear segments only, are plotted against time in 4.07 s time bins. Thick crosses denote the high-energy emission associated with the GF starting at t_0 and lasting ∼100 s. The background emission is represented by thin crosses and fitted with an appropriate smooth function (here a third-order polynomial), i.e. the dash–dotted curve. Consequently,

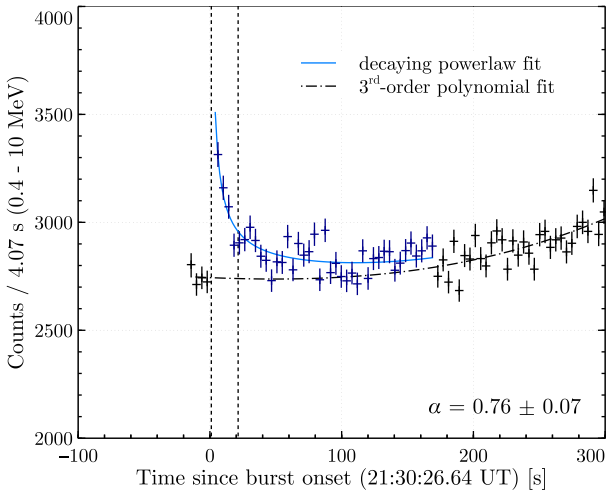

Figure 2. High-energy (0.4–10 MeV) counts (in the rear segments) against time since flare onset t_0 in time bins equal to the spacecraft rotation period, i.e. 4.07 s. A high-energy excess is present (thick crosses) for ∼100 s above the background (thin crosses). A third-order polynomial was fit to the background counts (dash–dotted curve) and a decaying PL $f(t) \propto t^{-\alpha}$ was fitted to the excess counts, i.e. the background-subtracted counts, with best-fitting parameter $\alpha = 0.76 \pm 0.07$ ($\chi^2_{\rm red} = 1.49$, 39 d.o.f.); the solid curve denotes the fit to the excess counts on top of the fit to the background. The spectrum has been generated from the time interval $t - t_0 = 1.07$–21.42 s, denoted by the vertical dashed lines. This figure should be compared to fig. 9 of Boggs et al. (2007).

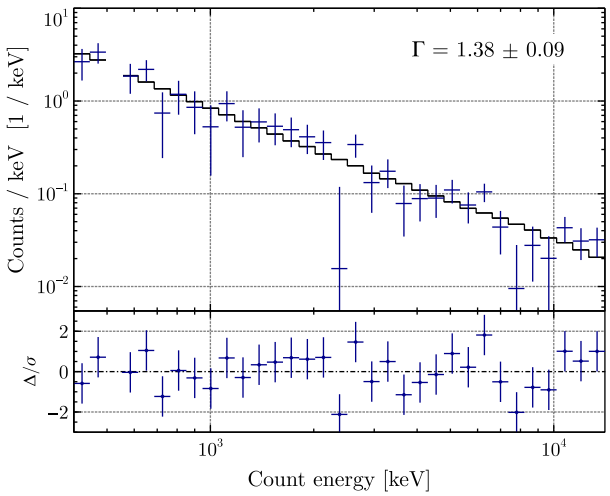

Figure 3. *RHESSI* count energy spectrum integrated over time interval $t - t_0 = 1.07$–21.42 s. The top panel shows the background-subtracted count distribution (crosses) and folded best-fitting source photon spectral model [step curve; $\Gamma = 1.38 \pm 0.09$ ($\chi^2_{\rm red} = 0.91$, 30 d.o.f.)] versus energy. The bottom panel shows the residuals. The energy bin including the 0.511 MeV line was omitted in determining the best-fitting photon spectral model.

the excess counts were fitted with a decaying PL $f(t) \propto t^{-\alpha}$ shown as the solid curve, with best-fitting parameter $\alpha = 0.76 \pm 0.07$ ($\chi^2_{\rm red} = 1.49$, 39 d.o.f.). This estimate is consistent with the one found by Boggs et al. (2007), i.e. $\alpha_{\rm B07} = 0.68 \pm 0.04$ ($\chi^2_{\rm red} = 1.63$, 39 d.o.f.). Fig. 2 should be compared to fig. 9 in Boggs et al. (2007).

A high-energy (0.4–15 MeV) background-subtracted count energy spectrum, shown in Fig. 3, was generated from the integrated

time interval[2] $t - t_0 = 1.07$–21.42 s (with $\Delta t_{\rm spec} \equiv 20.35$), denoted by the vertical dashed lines in Fig. 2. The top panel displays the count energy distribution dN/dE (crosses) of the counts recorded in the detectors rear segments and a folded best-fitting source photon spectral model (step curve). The latter was determined via a 'forward-fitting' procedure in XSPEC employing the appropriate instrumental response matrix for *RHESSI* (see Fig. B1) observing a source at 5° off-axis. The bottom panel shows the residuals of the fit. The bin containing the 511 keV line was excluded from the fitting procedure.

We assumed a simple PL model for the photon source spectrum $f(\varepsilon) = \mathcal{N}\varepsilon^{-\Gamma}$, where ε is the photon energy, and obtained the following best-fitting parameters: A normalization $\mathcal{N} = 4.58^{+5.07}_{-2.52}$ photons keV^{-1} cm^{-2} s^{-1} at 1 keV and photon index $\Gamma = 1.38 \pm 0.09$, with fit statistic $\chi^2_{\rm red} = 0.91$, 30 d.o.f. Accordingly, we may infer a photon flux integrated over the energy range 0.4–15 MeV of $F = (4.2 \pm 0.3) \times 10^{-6}$ erg cm^{-2} s^{-1}, with time-integrated fluence over $\Delta t_{\rm spec}$ of $\mathcal{F} = (8.6 \pm 0.6) \times 10^{-5}$ erg cm^{-2}. This result deviates from the fluence found by Boggs et al. (2007), i.e. $\mathcal{F} = (9.8 \pm 0.1) \times 10^{-5}$ erg cm^{-2}. We have not been able to fully determine the cause of this slight difference, since some relevant details of the data analysis done for the 2007 publication are not given. After consultation with the authors, however, we believe that the differences likely arise from the use of a distinct background extraction procedure resulting in a different background-subtracted source spectrum and adopting a slightly more up to date instrument response matrix that may modify the best-fitting parameters of the photon spectrum model, and consequently, the inferred photon fluence (Bellm, private communication).

Having confirmed the results of Boggs et al. (2007) regarding in particular the existence and general properties of the non-thermal hard component, we will now continue to investigate the pulsed emission. In particular, we would like to know how pulsed is the high-energy emission.

2.3 Pulsed emission

From Fig. 1, we notice that a strong pulsed fraction seems to be absent in the high-energy emission, as compared to the low-energy emission (Boggs et al. 2007). The degree to which the emission is pulsed in all of the bands will be important when we come to consider mechanisms that might generate the high-energy component. In this section, we will examine whether the apparent drop off in pulsed amplitude at the highest energies is genuine, or whether it could be an artefact of lower signal to noise in the higher energy band.

2.3.1 Issues with standard periodicity detection approaches

Comparing the pulsed fraction in low- and high-energy bands is not straightforward: whether the pulsed fraction is detected (or, indeed, detectable) depends on the details of the detector efficiency as a function of energy, the source energy spectrum, and the sky background in the detector as a function of energy. Here, we employ a simple empirical model to test whether the pulsed fraction is constant as a function of energy. Specifically, we extract light curves in four energy bands (25–40, 40–80, 80–250, and 250–15 000 keV) at a time resolution of 50 ms. We consider a segment between $t_0 + 4.2$ and $t_0 + 94.2$ s. The start time of this segment is set roughly by the end time of the first peak of the pulsating phase, since an instrumental artefact coincides with the first pulse maximum (see Fig. 1 and Appendix C). The end time is set approximately by the end of the detectable emission in the highest energy band. The complex time variability of the burst, including an overall decay, a re-brightening, and the changing shape of the pulse profile, lead to an equally complex power spectrum including a strong red noise component at low frequencies (see Fig. 4). Consequently, standard periodicity detection algorithms, which rest on the assumption of a white noise background, cannot be used (see e.g. Vaughan 2010; Huppenkothen et al. 2013).

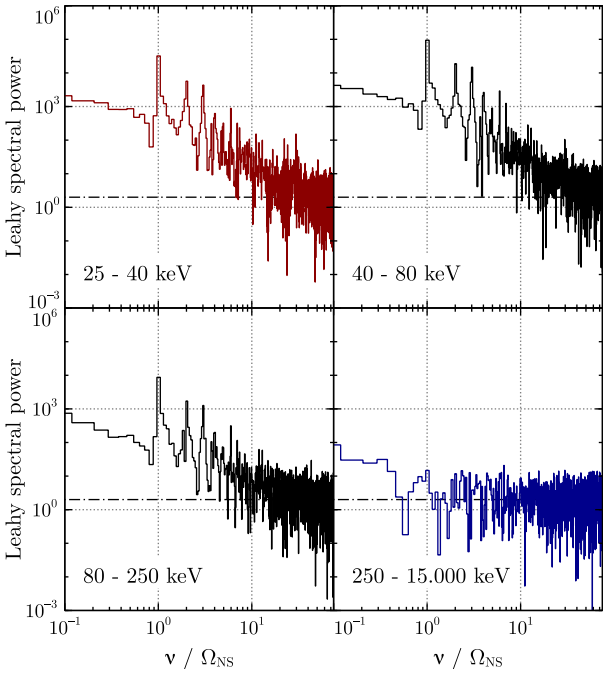

Figure 4. PSD plots of the separate energy bins (25–40, 40–80, 80–250, and 250–15 000 keV). The dash–dotted line denotes the Poisson noise level at $P = 2$. Notice the presence of a strong red noise component in three low-energy bins. The background dominates the highest energy bin, Fig. 2, so the red noise is much less pronounced. Furthermore, we can clearly distinguish the fundamental frequency at $\nu/\Omega_{\rm NS}$ in the low-energy bins (<250 keV). The high-energy bin (>250 keV) is dominated by noise, making it intricate to detect or negate the presence of any periodic variability.

2.3.2 Building template models for the observations

In order to model the observed emission in all four energy bands, we build a template pulse profile using the brightest band (40–80 keV). We first re-bin this light curve to a coarser resolution of 0.1 s and then fit the binned light curve with a cubic spline function, which allows us to interpolate a smooth version back to the original time resolution. We then extract an estimate of the total background by considering an interval of 26 s recorded before the burst in the same energy range and compute the count rate in that interval, assuming that all of the emission recorded in that interval is due to sky background. Under the additional assumption that the sky background is constant, we subtract off the counts per bin due to background from the template. By dividing this smooth version by the total number of source photons (i.e. the total number of photons

[2] Our time interval coincides exactly with the one chosen by Boggs et al. (2007). Note however that they round t_0 to the nearest whole second, i.e. $t_0^{\rm B07} = 21{:}30{:}26$ UT.

observed in this band, minus the total number of photons assumed to be due to background) in this energy band, we arrive at a template to use for further analysis.

In order to compare this template to the observations, we use the spectrum of the flare interval as well as the pre-flare interval to extract the integrated photon flux in the detector for source and background, respectively. The total photon flux from the flare interval includes contributions from both source and sky background. In order to get the source flux only, we subtract the time-scaled total number of photons expected from the sky background based on the pre-flare interval in the same energy band. We then construct a template light curve by multiplying the pulse template by the total source photons in each bin, and adding a constant sky background that integrates to the total sky background as extracted from the spectrum. This procedure results in a model light curve for each bin, appropriately scaled by the number of photons recorded in the detector, thus it takes the effects of the detector efficiency and the source energy spectrum into account.

2.3.3 Bayesian model comparison

The ultimate goal is to test whether we can confidently exclude a model where the pulsed fraction is constant with energy. Note that this is conceptually different from trying to detect whether there are any pulsations present in the data. In the latter case, we would presume no other knowledge of the problem and simply ask the question whether the data support the hypothesis of a (quasi-)periodicity in a given energy bin, without taking the other energy bins into account. Here, however, we are more interested in whether the data are consistent with a model where a periodicity is present in all four energy bins, but modulated by the changes in source spectrum and sky background as a function of energy, so that it might still go undetected with other period detection algorithms. To do so, we introduce an amplitude parameter A_i for each energy bin E_i, which scales the pulse profile. This allows us to set up two models encoding the hypotheses we are interested in. In model 1 (M_1), we assume the pulsed fraction is constant with energy, and any decrease in observed pulse fraction is caused by the energy dependence of source spectrum and sky background. Thus, in M_1 we define that the amplitudes A_i equal a single constant parameter C for all i, i.e. $A_i = C\,\forall i$. In model 2 (M_2), we allow the pulse amplitude to vary as a function of energy. Because we have no a priori knowledge of the functional form of this dependence, we allow the amplitude to vary independently in each energy bin. We parametrize the amplitude as $A_i = C + a_i\,\forall i$, which gives an additional set of N parameters $\{a_i\}_{i=1}^{N}$ for $N = 4$ light curves. While we could have parametrized A_i directly and reduced a parameter, this parametrization allows for the models to be nested (where the simpler model is a special case of the more complex model with $a_i = 0\,\forall i$), which is convenient for model comparison purposes.

Using these two parametrizations, we build two models for the observations in a Bayesian framework and use Markov Chain Monte Carlo (MCMC) to sample their parameters. Because the pulse shape may be mildly energy-dependent, we do not compare the light-curve template directly to the observed light curves, but instead produce power-density spectra (PDS) of the observed light curves as well as the model light curves. We add a PL component (with normalization $A_{\mathrm{PL},i}$ and index Γ_i) to each transformed model PDS to account for any red noise not modelled by the pulse shape itself as well as a constant w_i to account for Poisson statistics at high frequencies. This adds a set of 12 parameters $\{\Gamma_i, A_{\mathrm{PL},i}, w_i\}_{i=1}^{N}$ to each model.

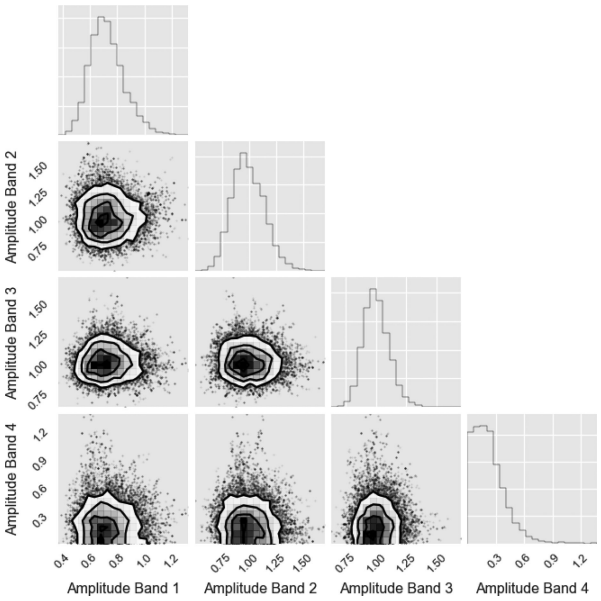

Figure 5. Posterior distributions for the pulse amplitudes in the four different bands. The distributions were calculated as $A_i = C + a_i$ for each band i and each sample in the MCMC chain.

Because the GF light curves were extracted in energy bands that do not overlap, we can consider them to be statistically independent, and can thus define a likelihood over all four light curves as the product of the individual likelihoods for each energy band. This, along with reasonable priors on the parameters (see Appendix A for details of the model and procedure), allows us to sample from the full model.

2.3.4 Results

We use MCMC in the form of EMCEE (Foreman-Mackey et al. 2013) to sample the posterior distributions of both M_1 and M_2 and find that the posterior distributions for M_1 and M_2 are well constrained. In order to compare M_1 and M_2 more formally, we exploit the nested nature of the models and use the Savage–Dickey density ratio (SDDR; defined in Appendix A) to approximate the ratio of marginalized posterior probability densities of M_1 to M_2 (i.e. the Bayes factor). Using the SDDR, we find a logarithmic Bayes factor of -1.6, corresponding to a 74 per cent probability of M_2 being true. Following Jeffrey's scale (Jeffreys 1998) and assuming equal prior probabilities for M_1 and M_2 (i.e. $p(M_1) = p(M_2) = 0.5$), we interpret this as very weak evidence in favour of the model with variable pulse amplitude. In Fig. 5, we present the posterior distributions for the pulse amplitudes. We note that while the posterior distributions for the pulse amplitudes are fairly wide, there is some indication that the pulse amplitude might not be constant here, too. In particular, the pulse amplitude for the highest energy bin is consistent with this emission not being pulsed. Furthermore, the emission in the lowest energy bin also appears to be less pulsed than the two middle bins.

We note, however, that this result depends quite strongly on prior choice: the Bayes factor trades off information content in the data with the volume of parameter space allowed by the prior. If the latter is very large for the additional parameters in M_2, the automatic penalty imposed may lead to a preference of the simpler model if the data are not exceptionally informative. Replacing the uniform prior for a_i with a Gaussian prior centred on zero with a standard deviation of 0.2 changes our conclusions quite drastically: in this case, there is moderate evidence for the model with constant pulse amplitude M_1

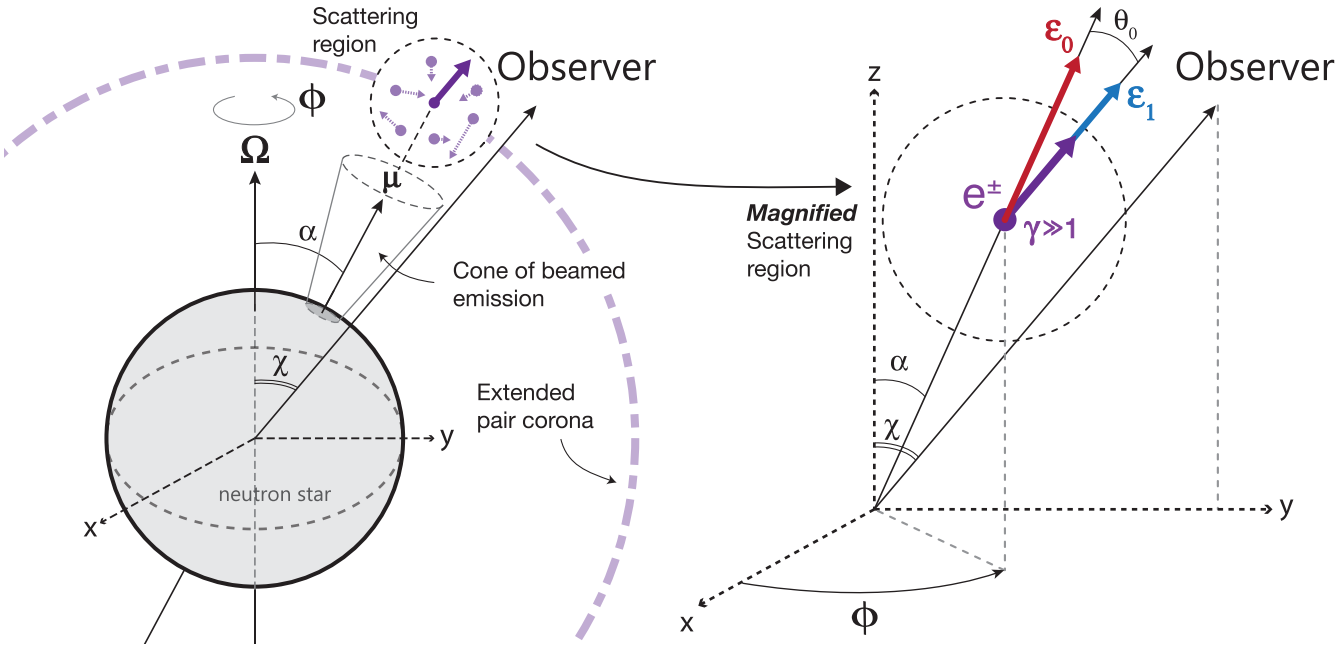

Figure 6. Schematic of the IC scattering configuration (not to scale). During the pulsation phase of the GF, a cone of beamed emission emerging from the evaporating fireball sweeps through the line of sight of the observer. Moreover, a portion of this anisotropic low-energy (i.e. <250 keV) emission proceeds to upscatter in a region that is part of an extended corona of isotropic relativistic pairs that envelops the NS, resulting in the high-energy spectral component (>400 keV). Here, $\boldsymbol{\varepsilon_0}$ and $\boldsymbol{\varepsilon_1}$, respectively, denote the incident photon unit vector (red thick arrow) and unit vector of the upscattered photon in the direction of the observer (blue thick arrow), χ is the angle between the rotation vector of the NS and the observer, $\cos\alpha = \boldsymbol{\mu}\cdot\boldsymbol{\Omega}$ denotes the angle between the rotation and magnetic dipole vector of the NS (or indeed the normal vector at the base of the fireball), θ_0 represents the incident photon angle, i.e. the angle between $\boldsymbol{\varepsilon_0}$ and the pair's direction of motion (in turn given by the purple thick arrow). Due to the rotation of the NS, the orientation of $\boldsymbol{\mu}(\phi)$ will vary periodically with respect to the observer, such that $\theta_0(\phi)$ will depend on the phase. From simulating IC spectra, we find that the photon spectral index Γ depends strongly on $\theta_0(\phi)$ (see Fig. 7) and will therefore also be phase-dependent.

(with posterior odds of 0.94). Given that even a fairly wide Gaussian prior can change the model's inference this drastically, we conclude that the data are not very informative. If it were, the likelihood would dampen the sensitivity of our conclusions to the choice of prior, and the model would converge to the same conclusions. This is also reflected in the likelihood ratio which only weakly prefers the model where the pulse amplitude depends on energy.

3 GLOBAL FLARE MODEL: A HIGHLY EXTENDED CORONA

In this section, we explore the model proposed by Boggs et al. (2007) to explain the high-energy non-thermal component during the peak decay. They hypothesize that this component originates in a highly extended corona, that has been driven by the hyper-Eddington luminosities, where the synchrotron cooling of the scattering particles is inefficient. The seed photons that are upscattered come from the jets of radiation that emanate from the base of the trapped pair-plasma fireball. They argue further that the lack of apparent pulsations in the high-energy light curve is consistent with this picture. Our analysis of the afterglow emission indeed shows that a model where the pulsed fraction decreases for the high-energy emission is preferred.

3.1 Inverse Compton scattering

Here, we wish to investigate whether the model proposed by Feroci et al. (2001) and Boggs et al. (2007) can reproduce the observed high-energy spectral component and furthermore whether such a process would isotropize or increase the degree of beaming of the beamed incident radiation emerging from the base of the fireball. We will make use of IC scattering calculations involving an anisotropic incident photon beam undertaken by Dubus, Cerutti & Henri (2008) and Cerutti (2010) in investigating the phase-dependent emission from γ-ray binaries. Here however we consider the following scenario, illustrated in Fig. 6. During the pulsation phase of the GF light curve, we consider the configuration wherein the pulsed soft X-ray emission is caused by a cone of beamed emission aligned with the magnetic dipole vector $\boldsymbol{\mu}$ of the NS[3] that moves in and out of the line of sight (parametrized by χ, i.e. the angle between the observer and rotational vector $\boldsymbol{\Omega}$ of the NS) as the underlying NS rotates. We subsequently assess the model where a portion of this beamed emission irradiates a *highly* extended corona comprising an isotropic distribution of pairs that envelops the NS. These pairs in turn upscatter, through IC scattering, the incident low-energy photons to higher energies (>tens of MeV).

We assume that the pairs are relativistic ($\gamma \gtrsim 10$), such that the outgoing photons will be beamed primarily, over an angle $\sim 1/\gamma$, in the direction of motion of the charged particles. Accordingly, we only observe the Comptonized emission scattering from charged particles that propagate in the direction of the observer. Consequently, we solely observe photons that have interacted with a charged particle at θ_0, which is given by

$$\cos\theta_0(\phi) = \cos\alpha\cos\chi + \sin\alpha\sin\chi\cos\phi \equiv \mu_0(\phi), \quad (1)$$

[3] The base of the fireball may not be aligned with the dipole vector of the NS. In that case, $\boldsymbol{\mu}$ represents the normal vector to the NS surface at the location of the base of the fireball.

where $\cos\alpha = \boldsymbol{\mu}\cdot\boldsymbol{\Omega}$ denotes the angle between the rotation and magnetic dipole vector of the NS, and ϕ represents the rotational phase of the NS.

In this configuration, the extended pair corona is hypothesized to be uniform. We will test this conjecture and discuss its validity in Sections 3.3.3 and 3.3.4, focusing mainly on its size constraints. The extended corona is illuminated at different longitudes, i.e. the scattering regions, as the soft X-ray beam sweeps round with ϕ. Accordingly, we approximate the incident photon spectrum as a blackbody distribution of constant temperature $k_{\rm B}T_{\rm bb}$. Furthermore, we assume that it is highly anisotropic, i.e. we model the emission cone as a entirely radially outward directed beam irradiating a scattering region from below at each instant in time. The seed photon distribution is therefore given by

$$\frac{{\rm d}n_{\rm X}}{{\rm d}\varepsilon_0} = \frac{2}{h^3c^3}\frac{\varepsilon_0^2}{\exp\left[\frac{\varepsilon_0}{k_{\rm B}T_{\rm bb}}\right]-1}, \tag{2}$$

where $n_{\rm X}$ is the soft X-ray photon number density, ε_0 is the incident photon energy, h is Planck's constant, and c is the speed of light. A fraction of these photons interacts kinematically with the relativistic pairs in the extended corona. We assume a simple isotropic PL energy distribution for the pairs up to a maximum energy[4] γ_+,

$$\frac{{\rm d}N_\pm}{{\rm d}\gamma} = \frac{1}{4\pi}K_\pm\gamma^{-p} \quad \gamma < \gamma_+, \tag{3}$$

where p denotes the spectral index of the pair energy distribution and $K_\pm$ represents the normalization in number of pairs per cm^2.

The differential cross-section of Compton scattering described by QED is given in the particle rest frame (PRF) by the Klein–Nishina (K-N) equation,

$$\frac{{\rm d}\sigma}{{\rm d}\Omega_1' d\varepsilon_1'} = \frac{r_e^2}{2}\left(\frac{\varepsilon_1'}{\varepsilon_0'}\right)^2\left(\frac{\varepsilon_1'}{\varepsilon_0'}+\frac{\varepsilon_0'}{\varepsilon_1'}-\sin^2\Theta'\right)\delta\left(\varepsilon_1'-\varepsilon_{1*}'\right), \tag{4}$$

where the primed quantities are defined in the PRF, $r_e \equiv e^2/(m_ec^2)$ is the classical electron radius, ε_1 is the energy of the outgoing photon, Θ is the angle between the incident and outgoing photon, δ denotes the Dirac distribution, and the Compton formula is given by

$$\varepsilon_{1*}' = \frac{\varepsilon_0'}{1+\frac{\varepsilon_0'}{m_\pm c^2}\left(1-\mu_\Theta'\right)}, \tag{5}$$

where $\mu_\Theta' = \cos\Theta' = \mu_1'\mu_0' + (1-\mu_1')^{1/2}(1-\mu_0')^{1/2}\cos(\phi_1'-\phi_0')$ and $\mu_i = \cos\theta_i$, with $i\in\{0,1\}$. We may translate the photon energies between the PRF and the lab frame through the relativistic Doppler shift equations:

$$\varepsilon_0' = \gamma\left(1-\beta\mu_0\right)\varepsilon_0, \tag{6}$$

$$\varepsilon_1' = \gamma\left(1-\beta\mu_1\right)\varepsilon_1, \tag{7}$$

where $\beta = v/c = (1-\gamma^{-2})^{1/2}$ is particle's velocity in units of c. Furthermore, the angles μ_i, with $i\in\{0,1\}$, translate according to the formula for the aberration of light,

$$\mu_i' = \frac{\mu_i-\beta}{1-\beta\mu_i}. \tag{8}$$

[4] For now, we have no physical reason to set a lower limit to the energy of the pairs. The distribution extends down to $\gamma_- = 1$. Our K-N kernel [equation (12)] and the assumption that we only observe upscattered photons from relativistic pairs that move in the direction of the observer, however both depend on an approximation that requires $\gamma \gg 1$. We address this assumption in Section 3.3.1.

The *normalized* anisotropic seed photon density for a monochromatic beam is given by

$$\frac{{\rm d}n}{{\rm d}\varepsilon d\Omega} = \delta\left(\varepsilon-\varepsilon_0\right)\delta\left(\mu-\mu_0\right)\delta\left(\phi-\phi_0\right), \tag{9}$$

which in the PRF becomes

$$\frac{{\rm d}n'}{{\rm d}\varepsilon' d\Omega'} = \gamma(1-\beta\mu)\delta\left(\varepsilon'-\varepsilon_0'\right)\delta\left(\mu'-\mu_0'\right)\delta\left(\phi'-\phi_0'\right). \tag{10}$$

In the lab frame, the anisotropic K-N kernel is then given by the following relation

$$\frac{{\rm d}N}{{\rm d}t d\varepsilon_1 d\Omega_1} = \frac{c}{\gamma^2(1-\beta\mu_1)}\iint\frac{{\rm d}n'}{{\rm d}\varepsilon' d\Omega'}\frac{{\rm d}\sigma}{{\rm d}\Omega_1' d\varepsilon_1'}d\varepsilon' d\Omega'. \tag{11}$$

Inserting equations (4) and (10), and making use of the following approximation $\mu_\Theta' \approx \mu_1'\mu_0'$ valid for $\gamma \gg 1$, one can write the anisotropic kernel as such

$$\frac{{\rm d}N}{{\rm d}t d\varepsilon_1} \simeq \frac{\pi r_e^2 c}{\gamma}\xi\frac{1-\beta\mu_0}{1-\beta\mu_1^*}\left\{1+\left(\frac{\mu_1^*-\beta}{1-\beta\mu_1^*}\mu_0'\right)^2 + \left(\frac{\gamma\varepsilon_1}{m_\pm c^2}\frac{1+\beta\mu_0'-(\beta+\mu_0')\mu_1^*}{\left\{1-\frac{\gamma\varepsilon_1}{m_\pm c^2}\left[1+\beta\mu_0'-(\beta+\mu_0')\mu_1^*\right]\right\}^{1/2}}\right)^2\right\}, \tag{12}$$

with

$$\xi \equiv \frac{\left\{1-\frac{\gamma\varepsilon_1}{m_\pm c^2}\left[1+\beta\mu_0'-\left(\beta+\mu_0'\right)\mu_1^*\right]\right\}^2}{\left|\beta\gamma\varepsilon_1+\frac{\varepsilon_1^2}{m_\pm c^2}\mu_0'\right|}, \tag{13}$$

and the outgoing photon angle

$$\mu_1^* \simeq \frac{1-\frac{\varepsilon_0}{\varepsilon_1}(1-\beta\mu_0)+\frac{\varepsilon_0}{\gamma m_\pm c^2}}{\beta+\frac{\varepsilon_0\mu_0}{\gamma m_\pm c^2}}. \tag{14}$$

To attain the emitted spectrum, we need to consider the seed photon energy distribution equation (2) and isotropic energy distribution of the scattering pairs equation (3) and proceed to numerically evaluate the following expression at each emitted photon energy ε_1,

$$\frac{{\rm d}N}{{\rm d}t d\varepsilon_1} = \iint\frac{{\rm d}N_\pm}{{\rm d}\gamma}\frac{{\rm d}n_{\rm X}}{{\rm d}\varepsilon_0}\frac{{\rm d}N}{{\rm d}t d\varepsilon_1}d\varepsilon_0 d\gamma. \tag{15}$$

The input parameters of the simulation are $T_{\rm bb}$, $K_\pm$, p, γ_+, and $\theta_0(\phi)$ where the latter may vary with the rotational phase ϕ of the NS, depending on fixed values for α and χ – see equation (1). The former parameters however are assumed to be constant, i.e. we assume a homogeneous energy distribution for the relativistic pairs in the extended corona, characterized by $K_\pm$, p, and γ_+, and that a given scattering region is always irradiated by the same incident photon spectrum, determined by $T_{\rm bb}$.

3.2 Results of the IC model

3.2.1 The IC spectra

We investigated the effect of varying the input parameters within a physically reasonable space has on the emitted spectrum, in the photon energy range 300–17 000 keV. We found that varying p changes the hardness of the emitted spectrum notably, whereas the remaining parameters only alter the normalization or display no apparent change in this energy range. For $\gamma_+ \lesssim 10^2$, the spectrum cuts off exponentially at roughly $\lesssim$20 MeV.

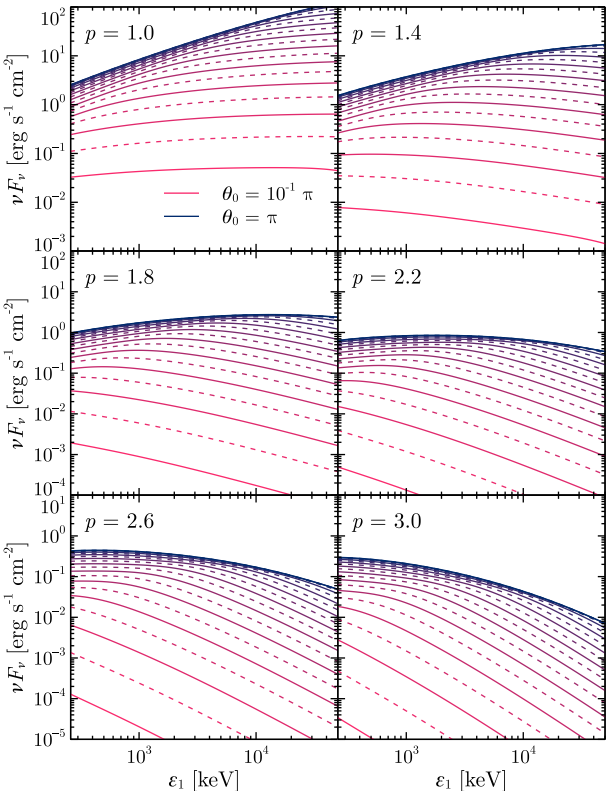

Figure 7. Simulated high-energy IC emission spectra. The separate graphs show the emission spectra for varying spectral index of the pair energy distribution p. The curves per graph represent the emission spectra for different values of the incident photon angle θ_0 ranging from 10^{-1} π to π in steps of 4.5×10^{-2} π; with $\gamma_+ = 10^4$ and $k_{\rm B}T_{\rm bb} = 10$ keV. Note that the spectra below $\lesssim$1 MeV, and in particular for small values of θ_0, may deviate due to the assumption that $\gamma \gg 1$.

Table 1. Results of the IC model fit to the observed *RHESSI* counts for fixed values of p and varying θ_0. Note that the best-fitting PL model was described by $\Gamma = 1.38 \pm 0.09$ with $\Delta\chi^2_{\rm red} = 0.91$ and 30 d.o.f.

p	θ_0/π	$\Delta\chi^2_{\rm red}$ (31 d.o.f.)
1.0	0.46	1.00
1.1	0.53	1.00
1.2	0.59	1.00
1.3	0.65	1.00
1.4	0.73	1.00
1.5	0.83	1.06[a]
1.6	0.83	1.18[a]
2.0	0.81	1.90[a]

Note. [a]Lowest obtainable values for $\Delta\chi^2$ for the respective values of p.

Results of the integration of equation (15) are shown in Fig. 7. Each subfigure exhibits a range of values for $\theta_0 = 10^{-1}\pi - \pi$ in steps of $4.5 \times 10^{-2}\pi$ for a set of values of the spectral index of the pair energy distribution $p \in \{1, 1.4, 1.8, 2.2, 2.6, 3\}$. Note that the slope of the emitted spectra increases as p decreases. We also see that the spectrum is harder with increasing incoming photon angle θ_0, i.e. as the collision with the particle becomes increasingly head-on.

We fit the IC model to the observed data for fixed values of p, varying θ_0. Best-fitting results are listed in Table 1. We find that

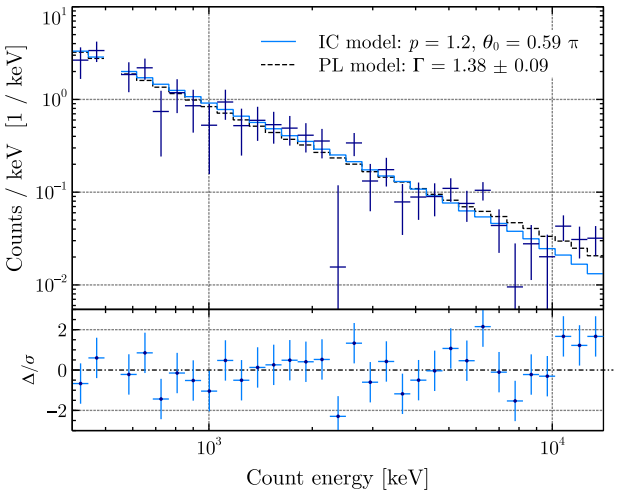

Figure 8. *RHESSI* count energy spectrum integrated over time interval $t - t_0 = 1.07$–21.42 s. The top panel shows the background-subtracted count distribution (crosses), best-fitting IC model [step curve; $p = 1.2$ and $\theta_0 = 0.59\pi$ ($\chi^2_{\rm red} = 1.00$, 31 d.o.f.)], and best-fitting PL photon spectral model [dashed step curve; $\Gamma = 1.38 \pm 0.09$ ($\chi^2_{\rm red} = 0.91$, 30 d.o.f.)] versus energy. The bottom panel shows the residuals of the IC model. The energy bin including the 0.511 MeV line was omitted in determining the best-fitting IC model.

we can attain $\Delta\chi^2_{\rm red} = 1.00$ for $p = 1$–1.4 and a poor fit for $p = 2$ (and $\theta_0 = 0.81\pi$), with $\Delta\chi^2_{\rm red} = 1.90$ and 31 d.o.f. For comparison, we plot the IC spectrum for $p = 1.2$ and $\theta_0 = 0.59\pi$ and the best-fitting PL in Fig. 8. If indeed the observed data are produced by Comptonized emission, we find that the energy distribution of the scatterers is required to be very hard to reproduce the observed spectrum, such that the acceleration mechanism must be very efficient $p \lesssim 1.5$. For instance, values of $p = 1$–1.2 may be attained through magnetic reconnection in the ultra-relativistic regime, i.e. where the energy density of the magnetic field dominates over the particle energy density $\epsilon_{\rm B}/\epsilon_p \gg 1$ (Sironi & Spitkovsky 2011; Guo et al. 2014). These particles may however cool due to strong synchrotron radiation, before being able to Compton upscatter the seed photons (see Section 3.3).

If we consider the case where $p = 1.2$, $\theta_0 = 0.59\pi$, and $\gamma_+ = 10^2$, we find that $K_\pm = (1.03 \pm 0.07) \times 10^{24}$ pairs cm^{-2}. Here, we have assumed a typical size for the NS, i.e. $R_{\rm NS} = 10^6$ cm and the source to be a distance $d = 8.7$ kpc from the observer (Bibby et al. 2008). Subsequently, with equation (3) we can estimate the required integrated energy of the pairs (with $1 < \gamma < 10^2$) in the scattering region,

$$E_\pm = m_\pm c^2 \int_{\gamma_-}^{\gamma^+} \gamma \frac{{\rm d}N_\pm}{{\rm d}\gamma} d\gamma \simeq 3.3 \times 10^{18} \text{ erg cm}^{-2}. \quad (16)$$

3.2.2 *The dependency of the IC spectrum on the phase*

When it comes to studying the pulsed fraction, comparing the simulated spectra to the data of the GF is hindered by the fact that we have no specific information on the angles χ and α, which both determine how θ_0 will vary with ϕ. What we do know however is that if the low-energy emission is strongly beamed and pulsed ($\alpha \notin \{0, \pi\}$), which it indeed should be for SGR 1806–20, then θ_0 will vary strongly as well according to the IC model. The strongest variation in the slope of the emitted spectrum due the variation of $\theta_0(\phi)$ will occur when $\alpha = \chi = \pi/2$.

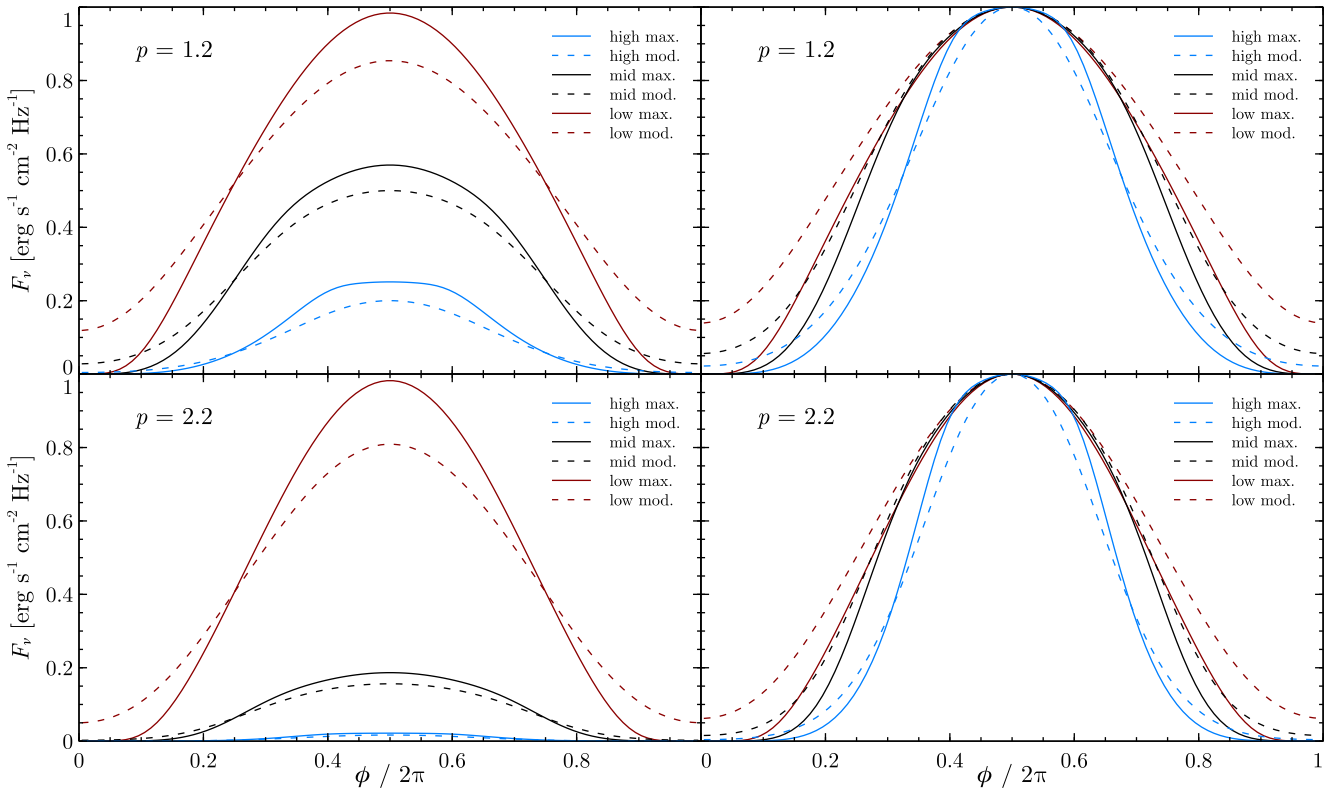

Figure 9. Simulated light curves of the Comptonized emission as a function of the NS rotational phase ϕ. We show the light curves for two values of the spectral PL index of the pair energy distribution $p \in \{1.2, 2.2\}$. Per plot the curves exhibit phase variability in three separate energy bands, i.e. low (260 keV $\leq \varepsilon_1^{\rm low} \leq$ 1.4 MeV), mid (1.4 MeV $< \varepsilon_1^{\rm mid} \leq$ 8.4 MeV), and high (8.4 MeV $< \varepsilon_1^{\rm high} \leq$ 50 MeV), and for two different dependencies of θ_0 on ϕ. For the latter, θ_0 may vary maximally (moderately) with ϕ, where $\cos\theta_0 = \cos\phi$ ($\cos_0 = 1/\sqrt{2}\cos\phi$). The left-hand panels show the relative flux of the separate energy bands; from which we see that the pulse amplitude decreases with energy, and decreases stronger for larger p. The right-hand panels show the fluxes normalized by their respective maximum value; from which we see that the anisotropy increases with energy, regardless the value of p.

In Fig. 9, we plot the simulated light curves as a function of the NS rotational phase ϕ. The plots correspond to two values of $p \in \{1.2, 2.2\}$. The solid and dashed curves respectively show a maximum and moderate dependence of the scattering angle on the phase, i.e. consecutively ($\chi = \pi/2$, $\alpha = \pi/2$) and ($\chi = \pi/2$, $\alpha = \pi/4$). Moreover, per plot the averaged flux of three distinct energy bands are shown, in the low (260 keV $\leq \varepsilon_1^{\rm low} \leq$ 1.4 MeV), mid (1.4 MeV $< \varepsilon_1^{\rm mid} \leq$ 8.4 MeV), high (8.4 MeV $< \varepsilon_1^{\rm high} \leq$ 50 MeV) range.

The left-hand panels show the relative flux of the separate energy bands and the right-hand panels show the fluxes normalized by their respective maximum value. We find that the pulse amplitude decreases with energy and that this effect is stronger at larger values for p. Moreover, we find that the anisotropy of the Comptonized emission increases with energy, regardless the value of p. The pulsed fraction remains very close to 1.0 in the case of maximum variability, yet does not become much less ($\gtrsim$0.85) in the case of moderate variability. Our analysis shows that the IC mechanism does not isotropize the thermal emission, as suggested by Boggs et al. (2007). In fact, the emission generated by this IC model remains strongly pulsed in the higher energy bands, contrary to what the data indicate.

3.3 Discussion and review of assumptions

3.3.1 Validity of the Klein–Nishina kernel

In deriving the K-N kernel given by equation (12), we made use of the approximation that $\gamma \gg 1$. Nevertheless, in generating the spectra we set our minimum particle energy at $\gamma_- = 1$. This however does not only affect the lower energy end of the resultant spectra (below 1 MeV, mainly for smaller values of θ_0), it also weakens the assumption that the Comptonized emission that we observe solely originates from kinematic interactions of seed photons with charged particles that propagate in the direction of the observer. If $\gamma \sim 1$, the outgoing photon is not necessarily beamed in the same direction as the motion of the charged particle. Hence, we may observe photons that have interacted with subrelativistic pairs, under a different incident angle than θ_0. This effectively means that the anisotropy will be somewhat reduced for the Comptonized emission at the lower energies, i.e. $\lesssim$1 MeV. None the less, the higher energies are much less affected by this assumption and will remain highly anisotropic as shown in Fig. 9.

3.3.2 A moving scattering region

We have assumed that the highly extended corona is stationary. In general, however we expect the corona to consist of an outflow; therefore, we can relax the hardness of the electron distribution by assuming that the scattering region is moving mildly relativistically away from the star. In the comoving frame, the energy of the thermal photons will be lower, such that the IC scattering is no longer in the K-N regime. Subsequently, we would still require a hard electron distribution with $p \lesssim 1.8$, yet much less hard than the value of $p \lesssim 1.4$ that corresponds to a stationary scattering region with respect to the observer. In the non-stationary case, we would expect the

hard emission to be as pulsed as the thermal emission, since both populations are boosted with respect to the observer. One would also expect the optical depth of the scattering region to decrease as it moves away if it also expands. The similar PL decay of the flux in the two energy regimes constrains changes in the optical depth.

3.3.3 IC cooling time and size of the corona

From equation (16), we found that the observed can be produced from IC scattering only if the total scattering region has approximately 3.3×10^{18} erg cm^{-2} of pairs with $1 < \gamma < 10^2$. Even though there may be higher energy particles, these none the less do not contribute much to the emission below 20 MeV. The total energy in the high-energy emission is $\sim 10^{42}$ erg assuming isotropic emission and a distance to the source of $d = 8.7$ kpc. This yields a scattering region radius of $r_{\rm sr} \sim 4.4 \times 10^4\, R_{\rm NS}$, which exceeds the light cylinder of the source, i.e. $R_{\rm lc} = c\,\Omega_{\rm NS}^{-1} \sim 3.6 \times 10^4\ R_{\rm NS}$. Only if $\gamma_+ \gtrsim 10^3$, do we find that $r_{\rm sr} < R_{\rm lc}$.

An important question is the cooling time of the scattering population. If the cooling time is much shorter than the duration of the high-energy excess emission, then the pairs must be continuously replenished. We can estimate the IC cooling time $\tau_{\rm c}^{\rm IC}$ by calculating the total energy column density of the pairs in the scattering region $E_\pm$ over the IC power per unit area ${\rm d}P_{\rm IC}/{\rm d}A$, i.e.

$$\tau_{\rm c}^{\rm IC} \sim E_\pm \left(\frac{{\rm d}P_{\rm IC}}{{\rm d}A}\right)^{-1}. \tag{17}$$

With equations (3) and (16), we find that we may write

$$E_\pm = \frac{m_\pm c^2 K_\pm}{4\pi}\left(\frac{\gamma_+^{-p+2} - \gamma_-^{-p+2}}{2-p}\right). \tag{18}$$

The IC power emitted by a single electron is given by

$$P_{\rm IC} = \frac{4}{3}\sigma_{\rm T} c \beta^2 \gamma^2 u_{\rm X}, \tag{19}$$

where $\sigma_{\rm T} \equiv (8\pi/3)\, r_e^2$ is the Thomson cross-section. We have made a modest approximation by using the Thomson cross-section rather than the K-N expression (4). Accordingly, we may infer the IC power per unit area of the scattering region as follows,

$$\begin{aligned}\frac{{\rm d}P_{\rm IC}}{{\rm d}A} &= \int_{\gamma_-}^{\gamma_+} P_{\rm IC}\frac{{\rm d}N_\pm}{{\rm d}\gamma}\,{\rm d}\gamma = \frac{\frac{4}{3}\sigma_{\rm T} c\, u_{\rm X} K_\pm}{4\pi}\int_{\gamma_-}^{\gamma_+}\beta^2\gamma^{-p+2}\,{\rm d}\gamma,\\ &\simeq \frac{\frac{4}{3}\sigma_{\rm T} c\, u_{\rm X} K_\pm}{4\pi}\left(\frac{\gamma_+^{-p+3} - \gamma_-^{-p+3}}{3-p}\right),\end{aligned} \tag{20}$$

where in the last step we assume that the scatterers are relativistic, i.e. $\beta \sim 1$. Consequently, we can write

$$\tau_{\rm c}^{\rm IC} \sim \frac{3 m_\pm c}{4\sigma_{\rm T} u_{\rm X}}\left(\frac{3-p}{2-p}\right)\frac{1}{\gamma_-}\left[\frac{\left(\frac{\gamma_\pm}{\gamma_-}\right)^{-p+2} - 1}{\left(\frac{\gamma_\pm}{\gamma_-}\right)^{-p+3} - 1}\right]. \tag{21}$$

The energy density of the incident X-ray emission can be estimated as

$$u_{\rm X} = \frac{L_{\rm X}}{\pi c R_{\rm NS}^2}\left(\frac{r_{\rm sr}}{R_{\rm NS}}\right)^{-2}, \tag{22}$$

where $L_{\rm X}$ denotes the (isotropic) X-ray flux at $R_{\rm NS}$, and $r_{\rm sr}$ represents the radial height of the scattering region.

Assuming $\gamma_+ \gg \gamma_-$, and adopting typical values for $p = 1.2$, $L_{\rm X} \sim 10^{42}$ erg s^{-1}, and $r_{\rm SR} \sim 10^4\, R_{\rm NS}$, we obtain an IC cooling time of,

$$\tau_{\rm c}^{\rm IC} \sim \frac{7 \times 10^{-4}}{\gamma_+}\left(\frac{r_{\rm sr}}{10^4 R_{\rm NS}}\right)^2 {\rm s}, \tag{23}$$

i.e. the pairs cool very rapidly through IC scattering.

Of course, this cooling mechanism would only affect the pairs that are illuminated by the beam of soft photons. We expect the pairs in these illuminated regions to be replenished high-energy particles in neighbouring regions. Observations of eruptive solar flares and magnetic reconnection models indicate that the total energy in this highly extended corona could be comparable to the energy released during the initial spike of the GF (Sironi & Spitkovsky 2014; Janvier, Aulanier & Démoulin 2015; Sironi, Giannios & Petropoulou 2016). Therefore, there should be sufficient total energy in the corona to power the late high-energy emission as long as other cooling mechanisms do not operate.

3.3.4 Synchrotron cooling time and lower limit to the size of the corona

Synchrotron emission might however cool the corona over the timescale of the high-energy emission. If we insist that the synchrotron cooling time is longer than 100 s, we can obtain a lower limit on the size of the corona and the energy contained within it. We can estimate the synchrotron cooling time $\tau_{\rm c}^{\rm syn}$ by taking equation (19) and substituting $u_{\rm X} \rightarrow u_{\rm B}$, where the latter is the magnetic energy density given by,

$$u_{\rm B} = \frac{B^2(r)}{8\pi} = \frac{B_0^2}{8\pi}\left(\frac{r}{R_{\rm NS}}\right)^{-6}, \tag{24}$$

assuming that the post-GF magnetic field resembles a dipole. We end up with the following estimate,

$$\tau_{\rm c}^{\rm syn} \sim \frac{4 \times 10^2}{\gamma_+}\left(\frac{r_{\rm sr}}{10^4 R_{\rm NS}}\right)^6 {\rm s}, \tag{25}$$

where we adopted a surface magnetic field strength of $B_0 \simeq 2 \times 10^{15}$ G (Nakagawa et al. 2009). Incidentally, the synchrotron cooling time will decrease in the case of a globally twisted magnetic field (Thompson et al. 2002).

The synchrotron cooling time of pairs with $\gamma_+ \geq 10^2$ can be stretched beyond 100 s only if the scattering region is larger than $1.7 \times 10^4\, R_{\rm NS}$. This means that the initial cloud of relativistic particles, that was presumably created near to the star during the initial spike of the GF, must expand by a factor more than $\sim 10^4$ without cooling due to IC scattering, synchrotron radiation or adiabatic expansion. The adiabatic effects alone reduce the Lorentz factor of the pairs by a factor of 10^4, dramatically increasing the energy requirements. Accounting for adiabatic losses alone would require an initial energy in relativistic particles at the reconnection event of $\sim 10^{46}$ erg, as much as the energy released in the GF itself. We must therefore conclude that the high-energy emission results from pairs that are continuously accelerated by the outflow rather than from pairs excited by the initial GF.

4 LOCAL FLARE MODEL: SHOCK ACCELERATION

The initial spike of the GF is expected to generate copious pairs and a large initial outflow. Outflows of material must persist throughout

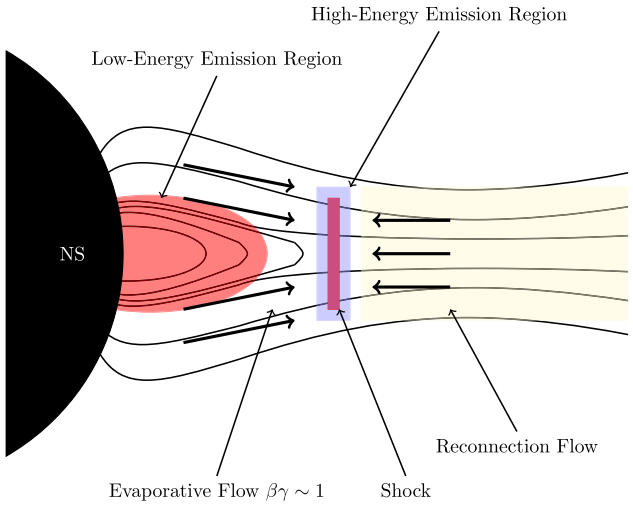

Figure 10. Local flare model in which the outflow generated near the surface forms a shock that accelerates particles and perhaps generates a magnetic field as well. The thickness of the high-energy emission region is limited by the cooling time.

the tail of the GF however, in order to collimate the low-energy emission and generate the prominent rotational pulsations (van Putten et al. 2016). These outflows are driven by the super-Eddington emission from the base of the trapped fireballs. We find that both the soft and hard photons decrease at a similar rate, i.e. the soft emission flux also decays as $f(t) \propto t^{-0.76}$ (see Section 2.2). This indicates a possible connection between the particle injection rate and the soft emission that originates from the outflow. We present a local emission model, inspired by the CSHKP model (after Carmichael 1964; Sturrock 1968; Hirayama 1974; Kopp & Pneuman 1976) for solar flares (e.g. Shibata & Magara 2011, for a review), in which the particles in the outflowing material can be accelerated sufficiently to replenish continuously the population of relativistic particles. This can be achieved if the outflow from near the surface of the NS collides with the exhaust of the reconnection region as depicted in Fig. 10, forming a shock that accelerates particles. Significant advances in the study of relativistic shocks have recently been made both theoretically and numerically through particle-in-cell simulations. In particular, their ability for particle acceleration and generating magnetic fields in the upstream region has been investigated (Sironi, Keshet & Lemoine 2015). It has been determined that the physics of relativistic shocks is strongly dependent on the value of the magnetization parameter $\sigma_{\rm m} \equiv 2u_{\rm B}/u_{\pm}$. Fundamentally, the conditions for the *Fermi* acceleration mechanism to operate are constrained by the orientation of the field with respect to the upstream flow in strongly magnetized shocks ($\sigma_{\rm m} \gtrsim 10^{-3}$ for pair dominated flows). Only for shocks where the orientation of the upstream magnetic field is near-parallel to the shock normal, can efficient particle acceleration occur. In weakly or unmagnetized shocks ($\sigma_{\rm m} \lesssim 10^{-3}$ for pair dominated flows) however, accelerated particles are more easily able to flow into the upstream region and excite electromagnetic plasma instabilities, which in turn produce magnetic structures that facilitate the *Fermi* acceleration mechanism.

4.1 Inverse Compton scattering

We first analyse the case in which the high-energy emission is produced by IC scattering of the low-energy photons by the particles accelerated in the shock. In this case, we can compare the fluence of the high-energy emission to that of the low-energy emission to obtain an estimate of the total energy in relativistic particles up to a Lorentz factor of 10^2. Although higher energy particles are likely to be present, they do not contribute to the emission <20 MeV. The total energy column density in the scatterers was determined in the previous section [equation (16)] to be

$$E_{\pm} = u_{\pm} l = 3.3 \times 10^{18}\ {\rm erg\ cm^{-2}}, \tag{26}$$

where here l is the thickness of the emission layer.

Meanwhile, the luminosity of the high-energy emission is about 3.8×10^{40} erg s^{-1}. Beyond about 350 stellar radii, IC cooling will dominate over synchrotron cooling, assuming that all of the magnetic field originates from the star. Rescaling equation (23), we find that in this case

$$\tau_{\rm c}^{\rm IC} \sim \frac{8 \times 10^{-7}}{\gamma_{+}} \left(\frac{r_{\rm sr}}{350\, R_{\rm NS}} \right)^2 {\rm s}\,, \tag{27}$$

and with $\gamma_{+} = 10^2$, we estimate a flux from the pairs at the source of

$$F_{\pm} \sim 4.1 \times 10^{26} \left(\frac{r_{\rm sr}}{350\, R_{\rm NS}} \right)^{-2} {\rm cm^{-2}\,erg\ s^{-1}}. \tag{28}$$

Combining this with the aforementioned luminosity yields the surface area of the scatterers

$$\Sigma_{\rm tot} \sim 9 \times 10^{13} \left(\frac{r_{\rm sr}}{350 R_{\rm NS}} \right)^2 {\rm cm^2}. \tag{29}$$

The combined cross-section of scatterers can only subtend a tiny fraction of the magnetosphere, i.e. roughly 6×10^{-5} of the sphere.[5]

We can also obtain an estimate of the minimal size of the scattering region by determining how far a relativistic particle can travel before cooling. The typical distance between scattering events is

$$\lambda_{\rm mfp} = \frac{\langle \epsilon_{\rm bb} \rangle}{\sigma_{\rm T} u_{\rm X}}, \tag{30}$$

where $\langle \epsilon_{\rm bb} \rangle \sim 27$ keV is the mean energy of a soft photon, for $k_{\rm B} T_{\rm bb} = 10$ keV. The typical number of scattering events is

$$N_{\rm scatt} = \frac{c\tau_{\rm c}^{\rm IC}}{\lambda_{\rm mfp}} \sim 1.7\, \frac{m_{\pm} c^2}{\gamma_{+} \langle \epsilon_{\rm bb} \rangle}, \tag{31}$$

with the relative change in the particle momentum of

$$\frac{\Delta p}{p} \sim \frac{\gamma_{+} \langle \epsilon_{\rm bb} \rangle}{m_{\pm} c^2}, \tag{32}$$

per scattering event. The particle essentially travels a straight path as it loses energy, so the minimum size of the scattering region is determined by the cooling time

$$c\tau_{\rm c}^{\rm IC} \sim \frac{2.4 \times 10^4}{\gamma_{+}} \left(\frac{r_{\rm sr}}{350 R_{\rm NS}} \right)^2 {\rm cm} = \frac{6.8 \times 10^{-5} r_{\rm sr}}{\gamma_{+}} \left(\frac{r_{\rm sr}}{350 R_{\rm NS}} \right). \tag{33}$$

Furthermore, the spectrum of scattered photons, even if the maximum Lorentz factor γ_{+} is large, will only extend to an energy

$$\epsilon_{\rm max} = \gamma_{\rm max} m_{\pm} c^2 = \gamma_{\rm max}^2 \langle \epsilon_{\rm bb} \rangle = \frac{m_{\pm}^2 c^4}{\langle \epsilon_{\rm bb} \rangle} \sim 10\ {\rm MeV} \tag{34}$$

[5] An equivalent way to look at this is to estimate the scattering optical depth. The typical photon increases its energy upon scattering by a factor of about 100, and the total luminosity in the soft component is 100 times larger than in the hard component, yielding a scattering optical depth of about 10^{-4}.

because above this energy the K-N cross-section becomes important.

In general, when a shock accelerates particles, it also generates a magnetic field such that $u_{\pm} \simeq u_{\rm B}$, where here the latter is the energy density of magnetic field generated in the shock (Sironi et al. 2015; Marcowith et al. 2016). Because we are examining a model where IC scattering dominates the high-energy radiation, we must also insist that $u_{\rm X} > u_{\rm B}$ and accordingly $u_{\rm X} > u_{\pm}$. Subsequently, we find that the thickness of the high-energy emission layer l must satisfy

$$l > \frac{u_{\pm} l}{u_{\rm X}} = 4 \times 10^4 \left(\frac{r_{\rm sr}}{350\, R_{\rm NS}} \right)^2 \ {\rm cm}, \tag{35}$$

where we made use of equations (22) and (26). For $\gamma_+ \sim 10^2$, which is necessary to account for the high-energy emission, this exceeds the cooling length by a factor of more than 100, creating difficulties for the IC model, if the particles are accelerated in a region thinner than l. If the region containing the relativistic particles is much thinner than this and magnetic field is also generated in the shock at a similar rate to the relativistic particles, synchrotron emission will dominate over IC.

Furthermore, given the analysis in Section 3, we expect IC scattering to yield a cut-off in the high-energy emission around 20–50 MeV and to result in pulsed high-energy emission. The analysis of the *RHESSI* data yields marginal evidence that the emission is at most weakly pulsed and there is no cut-off to the high-energy emission below 50 MeV.

4.2 Synchrotron radiation

We will now examine an alternative picture in which the high-energy emission results from synchrotron radiation. The magnetic field can be due to the star or generated in the shock itself (Sironi et al. 2015; Marcowith et al. 2016). In both cases, we will find that the cut-off in the high-energy emission may be small if the emission region is close to the star, but it is typically much larger if the shock is further away. Furthermore, if the magnetic field is generated in the shock itself, we expect it to be chaotic and the high-energy emission may be very weakly pulsed.

If the emission region is either close to the star (within 350 stellar radii) or thinner than a few hundred metres, synchrotron emission will indeed dominate over IC emission under the further assumption that the field strength decreases as a dipole from a surface field of about 2×10^{15} G. The pulsed fraction of the high-energy emission in this case will be low if the local magnetic field is chaotic. In principle, the magnetic field could become highly distorted either through reconnection or shocks. The field from the star at a distance of 350 $R_{\rm NS}$ is strong, but at about 5×10^7 G, it is less than the quantum critical field ($B_{\rm qed} \simeq 4.4 \times 10^{13}$ G), so synchrotron emission should proceed classically and extend into the MeV regime for electrons or positrons with $\gamma \sim 10^3$.

Rescaling equation (25), we note that at 350 $R_{\rm NS}$, the synchrotron cooling time is also short, i.e. $8 \times 10^{-7} \gamma_+^{-1}$s, which also requires that particles are continually accelerated to high energies; we therefore expect the high-energy flux to reflect the instantaneous particle injection rate. In the synchrotron picture, assuming that the particles are accelerated in a shock where the mildly relativistic outflow is halted, we would expect the particle injection rate to decrease in time as the soft flux does, and therefore expect the high-energy emission to decrease at the same rate as the soft emission.

Another observational feature that can pinpoint whether the emission is IC or synchrotron radiation is the cutoff energy. The *RHESSI* data do not indicate a cutoff energy <50 MeV. For synchrotron emission the cut-off depends on the strength of the magnetic field in the emission region; specifically, the maximum Lorentz factor $\gamma_{\rm co}$ of the pairs that emit classical synchrotron radiation is given by

$$\epsilon_{\rm co} = \gamma_{\rm co} m_{\pm} c^2 = \gamma_{\rm co}^2 \epsilon_{\rm cyc} = \frac{m_{\pm}^2 c^4}{\epsilon_{\rm cyc}} \tag{36}$$

where $\epsilon_{\rm cyc} = \hbar e B/(m_{\pm} c)$ is the non-relativistic cyclotron energy. For pairs with larger energy, the emission must be treated quantum mechanically. Therefore, there is a cut-off in the photon spectrum at this energy.

In order to estimate the cut-off for synchrotron emission, we have to estimate the magnetic field strength in the shock region. For this reason, we have to make some assumptions. The first one is obvious: we are analysing the case in which synchrotron dominates over IC, so we want $u_{\rm B} \gtrsim u_{\rm X}$, where $u_{\rm B}$ is the energy density of the magnetic field generated by the shock. We will consider $u_{\rm B} = a\, u_{\rm X}$, where $a \gtrsim 1$ is a boost parameter that depends on the distance of the shock region from the star.

The second constraint on the energy in the magnetic field is given by the assumption that the energy in the pairs accelerated by the shock and the energy in the magnetic field generated by the shock have to be the same order of magnitude, i.e. $u_{\pm} \sim u_{\rm B}$. We can estimate the energy in the pairs by multiplying the luminosity of the high-energy emission ($L_{\rm Hi} \sim 3.8 \times 10^{40}$ erg s^{-1}) by the synchrotron cooling time $\tau_{\rm c}^{\rm syn}$, which in turn is given by equation (21) and substituting $u_{\rm X} \rightarrow u_{\rm B}$ and setting $p = 1.8$. In equation (21), γ_+ and γ_- are defined as the maximum and minimum Lorentz factors for electrons emitting at the upper and lower limit of *RHESSI*'s band, respectively:

$$\epsilon_+ \approx 0.29 \frac{3}{2} \gamma_+^2 \epsilon_{\rm cyc} \sin\alpha \tag{37}$$

where $\epsilon_+ = 15$ MeV is the upper limit of *RHESSI*'s energy band, where we take $\sin\alpha \approx 0.5$ and the factor 0.29 is where the first synchrotron function $F(x)$ peaks (Rybicki & Lightman 1986). γ_- is defined in the same way, with $\epsilon_- = 0.4$ MeV (the lower limit of *RHESSI*'s high-energy band). The value of the limiting Lorentz factors depends on the strength of the magnetic field. The other missing piece of information is the volume of the emission region. The minimum thickness of the region is given by how far an electron moves in one cooling time. Assuming random walk, this is given by

$$l \gtrsim \sqrt{c \tau_{\rm c}^{\rm syn} \rho} \tag{38}$$

where $\rho = \gamma_- m_{\pm} c^2/(eB)$ is the Larmor radius.

We then indicate the surface area of the region by $q r_{\rm s}^2$, where $r_{\rm s}$ is the distance of the shock region from the star and $q < 1$. Our assumption that the energy in the magnetic field equals that in the pairs can then be translated in the following expression

$$\frac{L_{\rm Hi} \tau_{\rm c}^{\rm syn}}{u_{\rm B} l q r_{\rm s}^2} \simeq 1. \tag{39}$$

Accordingly we find,

$$u_{\rm B} \simeq 9 \times 10^{13} \left(\frac{q}{0.8} \right)^{-1} \left(\frac{r_{\rm s}}{350\, R_{\rm NS}} \right)^{-2} \ {\rm erg\ cm^{-3}}, \tag{40}$$

which corresponds to a magnetic field of

$$B \simeq 4.8 \times 10^7 \left(\frac{q}{0.8} \right)^{-1/2} \left(\frac{r_{\rm s}}{350\, R_{\rm NS}} \right)^{-1} \ {\rm G}. \tag{41}$$

This is given by imposing a minimum boost on the magnetic energy density compared to the energy density in the photons: $u_B = a\,u_X$, that does not depend on r_s

$$a \sim 1 \left(\frac{q}{0.8}\right)^{-1}. \quad (42)$$

Since in order for the emission to be dominated by synchrotron, a has to be greater than 1. Accordingly, we expect the area of the emission region to be smaller ($q < 0.8$). With these values, the minimum thickness of the emission region [equation (38)] becomes

$$l \simeq 0.35 \left(\frac{q}{0.8}\right)^{3/4} \left(\frac{r_s}{350\,R_{NS}}\right)^{3/2} \text{cm}. \quad (43)$$

This is assuming a zero thickness for the shock itself, so the thickness of the emission region is determined by the cooling length. Of course, there is still some arbitrariness in these estimates since the shock region can be thicker; equivalent to increasing a and decreasing the energy in the field, or have a smaller area (lower q), increasing the energy in the magnetic field. However, this picture is robust against changes in the parameters. For example, one could reduce the distance of the shock region from the star to $35R_{NS}$ and still have the field produced in the shock itself exceed the stellar dipole field, for $q < 8 \times 10^{-5}$, corresponding to a value of the boost parameter $a = 10^4$. If the shock region was much larger than this, then one would expect that the dipolar magnetic field may dominate over the one generated in the shock. In this case, synchrotron emission could still account for the high-energy photons, but it would be harder to explain a low pulse fraction with the more organized field configuration.

We find that the maximum Lorentz factor and, consequently, the cutoff energy, increase with the distance to the star:

$$\gamma_{co} \simeq 9.3 \times 10^5 \left(\frac{q}{0.8}\right)^{1/2} \left(\frac{r_s}{350\,R_{NS}}\right) \quad (44)$$

$$\epsilon_{co} \simeq 473 \left(\frac{q}{0.8}\right)^{1/2} \left(\frac{r_s}{350\,R_{NS}}\right) \text{GeV} \quad (45)$$

For example, in the case where the shock region is 10 times closer and much smaller so the shock-generated field still dominates over that of the star, ϵ_{co} is 10^3 times smaller at about 0.5 GeV. Measuring a cut-off in the *Fermi* energy band would point in the direction of a synchrotron emission process as the source of the high-energy emission and would give us information on the geometry of the emission region.

5 FLUENCE PREDICTION FOR *Fermi* GAMMA-RAY SPACE TELESCOPE

Fermi is designed to observe high-energy astrophysical phenomena over a large energy bandwidth with its two main instruments, the *GBM*, with energy bandpass from practically 10 keV to 38 MeV, and the *LAT*, covering an energy range ~80–10^4 MeV. There has been no magnetar GF during the lifetime of *Fermi*, which has been operational since 2008. It is currently the best instrument available to study the highest energy components of the emission should a magnetar GF occur and previous recurrence times suggest one could be imminent.

Here, we aim to predict the total number of counts that *Fermi* would detect in the event of a magnetar GF, similar to the 2004 December 27 event. With knowledge of the incident photon spectrum and flux as inferred from the *RHESSI* data, we can fold the obtained photon models (shown in Fig. 8) through the appropriate response (see Appendix B) using `fakeit` in XSPEC to find the count energy distribution that would be recorded by the respective instruments. The inferred photon spectral models, i.e. a PL (with $\Gamma = 1.38$, appropriate for synchrotron emission) and an IC model (with $p = 1.2$, $\theta_0 = 0.59\pi$, and $\gamma_+ = 10^6$), are based on a fit over the energy range 0.4–15 MeV. We know that below 0.4 MeV, the spectrum deviates from the deduced PL and IC spectrum. However, in the case of the PL spectrum, we cannot determine the cutoff energy from the *RHESSI* data; for the predictions we will assume that the PL extends into the *LAT* bandwidth. Boggs et al. (2007) note that they retrieve a slightly worse fit to the *RHESSI* count spectral data, when they introduce an exponential cut-off at >50 MeV, compared to the simple PL model. The simulated count data will provide us with an estimate of the number of counts that may be observed in the event of a GF. We will adopt the same amount of integration/observation time that was used in generating the *RHESSI* count spectrum, i.e. $\Delta t_{spec} = 20.35$ s.

Table 2. Predicted number of counts to be observed with the *Fermi* detectors (*LAT* and *GBM*) in the event of a GF comparable to the 2004 December 27 burst from SGR 1806–20. Estimates were made for two distinct inferred photon spectral models: a PL (with $\Gamma = 1.38$) and IC models (with $p = 1.2$, $\theta_0 = 0.59\pi$, and $\gamma = 10^6$). For comparison, *RHESSI* observed the latter at 5° off-axis and recorded ~2.1×10^3 counts in the energy range 0.4–15 MeV integrated over $\Delta t_{spec} = 20.35$ s. All reported numbers of counts are similarly the result of integrations over Δt_{spec}.

GRB identifier[a]	ζ_{LAT}	Model	$N_{LAT}/10^3$ (80–10^4) MeV	$N^b_{GBM}/10^3$ (0.4–38) MeV[c]
090510A	14°	PL	22.0 ± 0.7	4.8 ± 0.9
		IC	2.0 ± 0.2	4.5 ± 0.8
160509A	32°	PL	18.8 ± 0.8	4.9 ± 0.9
		IC	1.8 ± 0.2	4.5 ± 0.8
110721A	41°	PL	16.2 ± 0.6	4.5 ± 0.8
		IC	1.5 ± 0.2	4.4 ± 0.8
080916C	49°	PL	14.4 ± 0.7	4.7 ± 0.9
		IC	1.3 ± 0.2	4.7 ± 0.9
150210A	54°	PL	10.4 ± 0.5	4.1 ± 0.8
		IC	0.8 ± 0.1	4.1 ± 0.8

Notes. [a]These denote the names of the GRBs from which we used the instrument response files to generate the fake count spectra; obtained from the *Fermi GBM/LAT* GRB catalogue: http://fermi.gsfc.nasa.gov/ssc/observations/types/grbs/lat_grbs/index.php.
[b]These values represent the sum total of the simulated counts in the three NaI and BGO detectors where the GRB signal was the brightest.
[c]The lower energy limit of the *GBM* has been set to the lower limit of the observed non-thermal emission.

We obtained response matrices for the respective instruments from the online *Fermi GBM* and *LAT* γ-ray burst (GRB) catalogues.[6] We selected the instrument response files that were used in the spectral analysis of five bright GRBs, which respectively occurred at an angle ζ_{LAT} to the *LAT* boresight – see Table 2.

The *GBM* detector is composed of 12 Thallium Sodium Iodide crystals (NaI) and 2 Bismuth Germanate crystals (BGO, e.g. Meegan et al. 2009; Bissaldi et al. 2009) that provides full coverage of the non-occulted sky. We selected the response functions from three of the NaI and the BGO detectors where the signal was most prominent. We assume that in the event of a GF we can take the total sum of counts recorded in these four detectors as an estimate for the counts that the *GBM* would detect.

[6] Online *Fermi GBM* and *LAT* GRB catalogue: http://fermi.gsfc.nasa.gov/ssc/observations/types/grbs/lat_grbs/index.php.

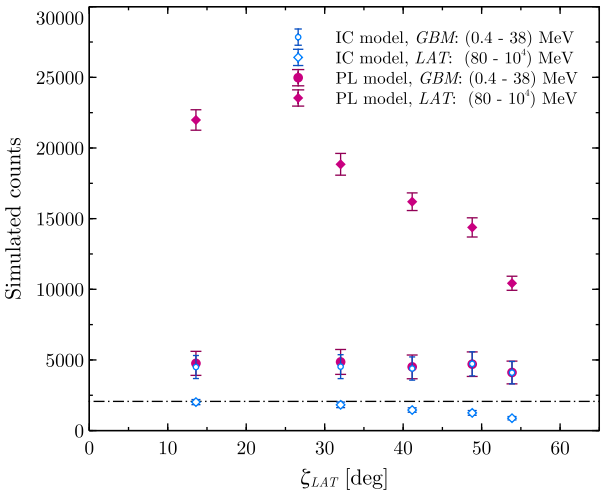

Figure 11. Simulated number of counts versus angle of *Fermi LAT* boresight $\zeta_{\rm LAT}$. We compare the results for the predicted number of counts in the separate *Fermi* instruments, i.e. the *GBM* and the *LAT*, based on the PL and IC models. By far the most counts are expected to be detected with the *LAT* if the PL extends up to 10^4 MeV. Moreover, we find that the predicted number of counts of the *LAT* are dependent on $\zeta_{\rm LAT}$ and decrease with increasing incident angle, whereas those for the *GBM* remain roughly constant. For comparison, the number of counts detected by *RHESSI* is shown by the horizontal dash–dotted line at $\sim 2.1 \times 10^3$.

Depending on data from the *GBM* or the *LAT*, the *GBM* may send a request for autonomous repointing (ARR) of the spacecraft. The *LAT* changes the observing mode to monitor the location of the transient in or near its FoV. After a pre-determined time (generally ∼2.5 h), the spacecraft will return to the scheduled mode. An ARR is performed within approximately ∼10 s (Meegan et al. 2009). Slewing of the *Fermi* spacecraft changes the photon angle of incidence $\zeta_{\rm LAT}$, which alters the instruments response function. We can estimate the advantageous effect of slewing towards the source by looking at the responses of GRBs that were observed at different incident angles, where a lower $\zeta_{\rm LAT}$ results in a higher number of observed counts with the *LAT* – see Fig. 11.

The results are summarized in Table 2. Compared to the number of high-energy counts observed with *RHESSI*, i.e. $\sim 2.1 \times 10^3$ counts, we find that the *LAT* would roughly observe an order of magnitude more counts in the case of a PL extending up to 10^4 MeV and a similar or less amount in the case of a IC photon spectrum. The total sum of the three NaI and one BGO detector of the *GBM* instrument would detect roughly 2–2.5 times the number of counts that *RHESSI* observed for both models. Setting the number of counts against the incident angle $\zeta_{\rm LAT}$, as shown in Fig. 11, we find that as expected for the *LAT* the number of counts decreases with increasing opening angle, whereas those for the *GBM* remain approximately constant.

In any case, we expect that the *Fermi* data will by virtue of the increase in the observed number of counts, allow more stringent tests of the physical mechanism that generates the high-energy emission, in particular the IC model.

6 CONCLUSION

In this work, we aimed to reproduce the results of the *RHESSI* data analysis done by Boggs et al. (2007) on the high-energy excess emission observed during the GF of SGR 1806–20 on 2004 December 27. Moreover, we set out to study the proposed underlying physical mechanism that may produce such high-energy emission, i.e. IC scattering in a highly extended relativistic pair corona, and investigate the constraints it places on such extraordinary phenomena.

We were able to confirm the earlier results of Boggs et al. (2007) regarding the general properties of the high-energy emission. Crucial however to testing the aforementioned model was to determine whether the high-energy component (>250 keV) could be the result of a pulsed source as is apparent for the low-energy emission (<250 keV). Using more detailed statistical analysis/robust method, we have shown that the existing data from *RHESSI* are consistent with a model where the high-energy emission is not pulsed, but the data are only weakly constraining.

Subsequently, we have shown that IC scattering of a highly anisotropic beam of soft radiation emerging from a trapped fireball could generate this high-energy emission given a suitable population of scatterers. The IC model fits the observed counts best for $p = 1$–1.4, i.e. for a scattering population that has been accelerated (very) efficiently. The origin of the scattering population however remains an open question. If the scattering population is moving mildly relativistically or if the emission is produce by synchrotron radiation, the particle distribution is a bit softer $p \approx 1.8$. In either case, the relativistic particles have to be replenished continuously to account for the emission. The current data are insufficient to decide the issue; better constraints on the time decay of the hard emission and a determination of whether it is pulsed or whether it cuts off below 50 MeV would help to decide the issue. We find that according to the IC model, the outgoing high-energy emission will not be isotropized in the process, in fact a significant pulsed fraction is to be expected for the Comptonized emission if this is also observed for the low-energy emission. Furthermore in the IC model, we also expect the emission to cut-off below 50 MeV.

Next, we examined a local flare model where synchrotron emission dominates the hard band. Synchrotron will dominate if the emission region is within about 350 stellar radii or if it is thinner than a few hundred metres. If the magnetic field is generated in a shock along with the relativistic pairs, the synchrotron emission may only be weakly pulsed and can continue into the GeV regime without a cut-off.

Fermi LAT/GBM is very well placed to detect the next GF. We have estimated that, depending on the model for the production of the high-energy emission, *Fermi GBM* and *LAT* may, respectively, detect approximately 2–2.5 times and ∼1–10 times the number of counts that *RHESSI* observed in the event of a similar GF to the one from SGR 1806–20. With better observations, i.e. more observed counts and in a broader high-energy range, we may be able to observe and analyse in more detail properties of the Comptonized or synchrotron emission, thereby placing tighter constraints on the models for the high-energy emission of magnetar GFs.

ACKNOWLEDGEMENTS

CE and ALW acknowledge support from NOVA, the Dutch Top Research School for Astronomy. EB acknowledges the Italian 'Fondo di Sviluppo e Coesione 2007–2013 – APQ Ricerca Regione Puglia – Future In Research'. CO, IC, and JSH acknowledge support from the Natural Sciences and Engineering Research Council of Canada, the Canadian Foundation for Innovation, and the British Columbia Knowledge Development Fund. CO also acknowledges support from the Japanese Ministry of Education, Culture, Sports, Science and Technology. We would like to thank Eric Bellm, Steven

Boggs, Gordon Hurford, and David Smith for helpful discussions and advice relating to the *RHESSI* GF data.

REFERENCES

Abdo A. A. et al., 2010, ApJ, 725, L73
Atwood W. B. et al., 2009, ApJ, 697, 1071
Baring M. G., Harding A. K., 2007, Ap&SS, 308, 109
Baring M. G., Gonthier P. L., Harding A. K., 2005, ApJ, 630, 430
Beloborodov A. M., 2012, ApJ, 762, 13
Bhat P. N. et al., 2016, ApJS, 223, 1
Bibby J. L., Crowther P. A., Furness J. P., Clark J. S., 2008, MNRAS, 386, L23
Bissaldi E. et al., 2009, Exp. Astron., 24, 47
Boggs S. E., Zoglauer A., Bellm E., Hurley K., Lin R. P., Smith D. M., Wigger C., Hajdas W., 2007, ApJ, 661, 458
Cameron P. B. et al., 2005, Nature, 434, 1112
Carmichael H., 1964, A Process for Flares. NASA Special Publication, Washington, DC
Collazzi A. C. et al., 2015, ApJS, 218, 1
den Hartog P. R., Hermsen W., Kuiper L., Vink J., in 't Zand J. J. M., Collmar W., 2006, A&A, 451, 587
den Hartog P. R., Kuiper L., Hermsen W., Kaspi V. M., Dib R., Knödlseder J., Gavriil F. P., 2008a, A&A, 489, 245
den Hartog P. R., Kuiper L., Hermsen W., 2008b, A&A, 489, 263
Dickey J. M., 1971, Ann. Math. Stat., 42, 204
Dubus G., Cerutti B., Henri G., 2008, A&A, 477, 691
Enoto T., Makishima K., Nakazawa K., Kokubun M., Kawaharada M., Kotoku J., Shibazaki N., 2011, PASJ, 63, 387
Feroci M., Frontera F., Costa E., Amati L., Tavani M., Rapisarda M., Orlandini M., 1999, ApJ, 515, L9
Feroci M., Hurley K., Duncan R. C., Thompson C., 2001, ApJ, 549, 1021
Foreman-Mackey D., Hogg D. W., Lang D., Goodman J., 2013, PASP, 125, 306
Frail D. A., Kulkarni S. R., Bloom J. S., 1999, Nature, 398, 127
Frederiks D. D., Golenetskii S. V., Pal'shin V. D., Aptekar R. L., Ilyinskii V. N., Oleinik F. P., Mazets E. P., Cline T. L., 2007, Astron. Lett., 33, 1
Götz D., Mereghetti S., Tiengo A., Esposito P., 2006, A&A, 449, L31
Granot J. et al., 2006, ApJ, 638, 391
Guo F., Li H., Daughton W., Liu Y.-H., 2014, Phys. Rev. Lett., 113, 155005
Hirayama T., 1974, Sol. Phys., 34, 323
Huppenkothen D. et al., 2013, ApJ, 768, 87
Hurley K., Cline T., Mazets E., Barthelmy S., Butterworth P., 1999, Nature, 397, 41
Hurley K. et al., 2005, Nature, 434, 1098
Janvier M., Aulanier G., Démoulin P., 2015, Sol. Phys., 290, 3425
Jeffreys H., 1998, The Theory of Probability. Oxford Univ. Press, Oxford
Kopp R. A., Pneuman G. W., 1976, Sol. Phys., 50, 85
Kuiper L., Hermsen W., Mendez M., 2004, ApJ, 613, 1173
Kuiper L., Hermsen W., den Hartog P. R., Collmar W., 2006, ApJ, 645, 556
Li J., Rea N., Torres D. F., de Ona-Wilhelmi E., 2016, ApJ, 835, 30
Marcowith A. et al., 2016, Rep. Prog. Phys., 79, 046901
Mazets E. P., Golenetskii S. V., 1981, Ap&SS, 75, 47
Mazets E. P. et al., 1979, SvA Lett., 5, 163
Meegan C. et al., 2009, ApJ, 702, 791
Mereghetti S., Götz D., Mirabel I. F., Hurley K., 2005, A&A, 433, L9
Molkov S., Hurley K., Sunyaev R., Shtykovsky P., Revnivtsev M., Kouveliotou C., 2005, A&A, 433, L13
Nakagawa Y. E. et al., 2009, PASJ, 61, 387
Nobili L., Turolla R., Zane S., 2008a, MNRAS, 386, 1527
Nobili L., Turolla R., Zane S., 2008b, MNRAS, 389, 989
Pavan L., Turolla R., Zane S., Nobili L., 2009, MNRAS, 395, 753
Pedregosa F. et al., 2011, J. Mach. Learn. Res., 12, 2825
Rybicki G. B., Lightman A. P., 1986, Radiative Processes in Astrophysics. Wiley-VCH, Weinheim, Germany, p. 400
Shibata K., Magara T., 2011, Living Rev. Sol. Phys., 8, 6
Sironi L., Spitkovsky A., 2011, ApJ, 741, 39
Sironi L., Spitkovsky A., 2014, ApJ, 783, L21
Sironi L., Keshet U., Lemoine M., 2015, Space Sci. Reviews, 191, 519
Sironi L., Giannios D., Petropoulou M., 2016, MNRAS, 462, 48
Smith D. M. et al., 2002, Sol. Phys., 210, 33
Sturrock P. A., 1968, in Kiepenheuer K. O. eds, IAU Symp. 35, Structure and Development of Solar Active Regions. D. Reidel, Dordrecht, p. 471
Sturrock P. A., Harding A. K., Daugherty J. K., 1989, ApJ, 346, 950
Şaşmaz Muş S., Göğüş E., 2010, ApJ, 723, 100
Thompson C., Beloborodov A. M., 2005, ApJ, 634, 565
Thompson C., Duncan R. C., 1995, MNRAS, 275, 255
Thompson C., Duncan R. C., 2001, ApJ, 561, 980
Thompson C., Lyutikov M., Kulkarni S. R., 2002, ApJ, 574, 332
Turolla R., Zane S., Watts A. L., 2015, Rep. Prog. Phys., 78, 116901
van Putten T., Watts A. L., D'Angelo C. R., Baring M. G., Kouveliotou C., 2013, MNRAS, 434, 1398
van Putten T., Watts A. L., Baring M. G., Wijers R. A. M. J., 2016, MNRAS, 461, 877
Vaughan S., 2010, MNRAS, 402, 307
Viganò D., Parkins N., Zane S., Turolla R., Pons J. A., Miralles J. A., 2012, J. Phys.: Conf. Ser., 342, 012013
Woods P. M., Kouveliotou C., Finger M. H., Goegues E., Wilson C. A., Patel S. K., Hurley K., Swank J. H., 2007, ApJ, 654, 470
Zane S., Turolla R., Nobili L., Rea N., 2011, Sun and Similar Stars/Cosmic Ray Spectra and Composition, 47, 1298

APPENDIX A: GIANT FLARE PULSE MODEL

We use Bayes rule to build a posterior probability distribution for the power spectral densities (PSDs) of all four energy bins simultaneously:

$$p(\theta \mid \boldsymbol{D}, \alpha, M) = \frac{p(\boldsymbol{D} \mid \theta, \alpha, M) p(\theta \mid \alpha, M)}{p(\boldsymbol{D} \mid \alpha, M)}\,, \tag{A1}$$

where θ denotes a vector of all model parameters, $\boldsymbol{D} = \{D_i\}_{i=1}^{N}$ is the set of power spectra extracted from each energy bin, α denotes a set of hyper parameters for the prior distributions on θ (see Appendix A2 below for details), and M denotes any additional model assumption.

In addition, we denote $\mathcal{L}(\theta) = p(\boldsymbol{D} \mid \theta, \alpha M)$ as the likelihood, i.e. the probability of the data given the model (parameters), $\pi(\theta) = p(\theta \mid \alpha, M)$ as the prior probability of the parameters θ, and $p(\boldsymbol{D} \mid \alpha, M) = \int_\Omega p(\boldsymbol{D} \mid \theta, \alpha, M) p(\theta \mid \alpha, M) d\Omega$ is the marginal likelihood or evidence, i.e. the posterior integrated over the full-parameter space Ω allowed by the prior.

We use an exponential likelihood appropriate for modelling power spectra in the absence of significant dead time. For a single power spectrum D_i in energy bin i with M powers $\{P_{i,j}\}_{i=1,j=1}^{N,M}$ at each frequency ν_j we have:

$$\mathcal{L}_i(\theta) = p(D_i \mid \theta, \alpha M) = \prod_{i=1}^{M} \frac{1}{\hat{P}_{i,j}(\theta)} \exp\left(\frac{P_{i,j}}{\hat{P}_{i,j}(\theta)}\right), \tag{A2}$$

where $\hat{P}_{i,j}$ denotes the model power at frequency ν_j in energy bin i. We assume that the observed power spectra in different energy bins are statistically independent; this assumption is valid as long as the photon detection process can be assumed to be largely energy-independent (i.e. the probability of detecting a photon of energy E_1 does not directly depend on the probability of having previously detected a photon of energy E_2) and our energy bins do not overlap. In this case, the joint likelihood for N power spectra becomes:

$$p(\boldsymbol{D} \mid \theta, \alpha, M) = \prod_{i=1}^{N} \mathcal{L}_i(\theta)\,. \tag{A3}$$

Model comparison can now be performed via comparison of the marginal likelihoods. For two models M_1 and M_2 with priors $p(M_1)$ and $p(M_2)$, and marginal likelihoods $p(\boldsymbol{D} \mid M_1)$ and $p(\boldsymbol{D} \mid M_2)$, we can define

$$\frac{p(M_1 \mid \boldsymbol{D})}{p(M_2 \mid \boldsymbol{D})} = \frac{p(\boldsymbol{D} \mid M_1)}{p(\boldsymbol{D} \mid M_2)} \frac{p(M_1)}{p(M_2)}. \tag{A4}$$

In practice, the posterior probability distribution is often not analytical, and thus the marginal likelihood difficult or expensive to compute. However, the expression can be simplified if the models M_1 and M_2 are nested, that is, if M_1 is a special case of M_2. Suppose M_1 only has parameters θ, and M_2 has parameters $\{\theta, \phi\}$, and M_1 is a special case of M_2 if $\phi = \phi_0$, then the Bayes factor $B_{12} = \frac{p(\boldsymbol{D} \mid M_1)}{p(\boldsymbol{D} \mid M_2)}$ reduces to the SDDR,

$$B_{12} = \frac{p(\phi \mid \boldsymbol{D}, M_2)}{p(\phi \mid \alpha, M_2)}\Big|_{\phi=\phi_0}, \tag{A5}$$

where we have integrated $p(\phi \mid \boldsymbol{D}, M_2) = \int_\Omega p(\theta, \phi \mid \boldsymbol{D}, \alpha, M_2) \mathrm{d}\theta$ and Ω denotes the total prior volume spanned by the parameters θ (Dickey 1971).

In practice, we compute the SDDR by first sampling from M_2. We then marginalize over all nuisance parameters (here all parameters in both M_1 and M_2) and approximate the marginalized posterior distribution $p(\{a_i\}_{i=1}^N \mid \boldsymbol{D}, M_2)$ using a kernel density estimate as implemented in *scikit-learn* (Pedregosa et al. 2011). This allows us to compute the posterior probability where $a_i = 0 \,\forall i$ as required in equation (A5).

A1 The model

We model the PDS in each energy i bin with equation (1) the Fourier-transformed template pulsed light curve, scaled appropriately to the photon flux in that energy band from both source and background, (2) a PL component with parameters Γ_i (index) and $A_{\mathrm{PL},i}$ (amplitude) to account for any red noise not accounted for in the pulse profile, (3) a constant w_i to account for the flat white noise component visible in the PSDs at high frequencies. These parameters are shared between M_1 and M_2. In addition, we consider a scaling factor A_i applied to the pulse profile light curve before Fourier transforming in each energy bin, which accounts for any energy-dependent differences in the pulsed fraction.

For the simpler model M_1, the scaling factor A_i is constant with energy and thus equal for all energy bins, i.e. $A_1 = A_2 = \ddots = A_N = C$. The more flexible model M_2 is parametrized as $A_i = C + a_i$, where C is a constant scaling shared by all energy bins, and a_i is an offset in energy bin i from that shared scaling factor. This parametrization is convenient, because the models are nested such that we can recover M_1 by setting $a_i = 0 \,\forall i$. Under the assumption that the priors for a_i and C are separable, we can use the SDDR in comparing the two models. Our full set of parameters for M_1 is $\theta_1 = \{\{\Gamma_i\}_{i=1}^N, \{A_{\mathrm{PL},i}\}_{i=1}^N, \{w_i\}_{i=1}^N, C\}$, and for M_2 we have $\theta_2 = \{\{\Gamma_i\}_{i=1}^N, \{A_{\mathrm{PL},i}\}_{i=1}^N, \{w_i\}_{i=1}^N, C, \{a_i\}_{i=1}^N\}$.

A2 Priors

We place largely non-informative priors on our parameters, summarized in Table A1. In addition to the individual parameter priors, we impose two additional restrictions. First, for both models we are requiring that all powers in each model power spectrum $\{\hat{P}_{i,j}\}_{i=1,j=1}^{N,M} > 0$, a requirement imposed by the definition of the power spectrum as the square of the real part of the Fourier transform.

In order to encode the second assumption as a prior, we introduce the model powers at frequency ν_j in energy bin i, $\{\hat{P}_{i,j}\}_{i=1,j=1}^{N,M}$ as latent variables in our model, such that our posterior for M_1 becomes

$$p(\{\hat{P}_{i,j}\}_{i=1,j=1}^{N,M}, \theta_1 \mid \boldsymbol{D}, \alpha, M_1) = \frac{p(\boldsymbol{D} \mid \{\hat{P}_{i,j}\}_{i=1,j=1}^{N,M}, \theta_1, M_1) p(\theta_1 \mid \alpha, M_1) p(\{\hat{P}_{i,j}\}_{i=1,j=1}^{N,M} \mid \alpha, M_1)}{p(\boldsymbol{D} \mid M_1)}. \tag{A6}$$

Because the powers $\{\hat{P}_{i,j}\}_{i=1,j=1}^{N,M}$ are uniquely determined once the parameters θ_1 are known, the prior is a Dirac delta function around the function values, unless any of those function values are negative:

$$p(\{\hat{P}_{i,j}\}_{i=1,j=1}^{N,M} \mid \alpha, M_1) = \begin{cases} \delta(P_{i,j} - \hat{P}_{i,j}), & \text{if } \hat{P}_{i,j} > 0 \,\forall i, j. \\ 0, & \text{otherwise.} \end{cases} \tag{A7}$$

In practice, this definition of the prior on the latent variables as a delta function allows for straightforward marginalization over these latent variables in order to compute the posterior distribution over parameters θ alone.

APPENDIX B: INSTRUMENT RESPONSES

The *RHESSI* response matrix displayed in Fig. B1 represents the response of the detector's rear segments at 5° incidence angle and was generated by E. Bellm. We obtain an effective area curve by integrating the response matrix along the axis of the count energies. The effective area indicates the instrument's overall sensitivity to a given photon energy.

Table A1. Overview of the priors used in the Bayesian model.

Parameter	Meaning	Probability distribution
Shared parameters		
Γ_i	PL index	Uniform(0, 4)
$\log A_{\mathrm{PL}}$	PL amplitude	Uniform(−10, 10)
C	Constant parameter scaling	Normal(1, 0.5)
w_i	Poisson noise amplitude	$\mathrm{Truncated}_{\mathrm{Normal}}(0, 0.1, 0.0, \infty)^a$
Variable pulse fraction model M_2		
a_i	Scaling offsets	Uniform(−2, 2)

Notes. An overview over the model parameters with their respective prior probability distributions.
[a]Truncated normal distribution with lower bound and no upper bound.

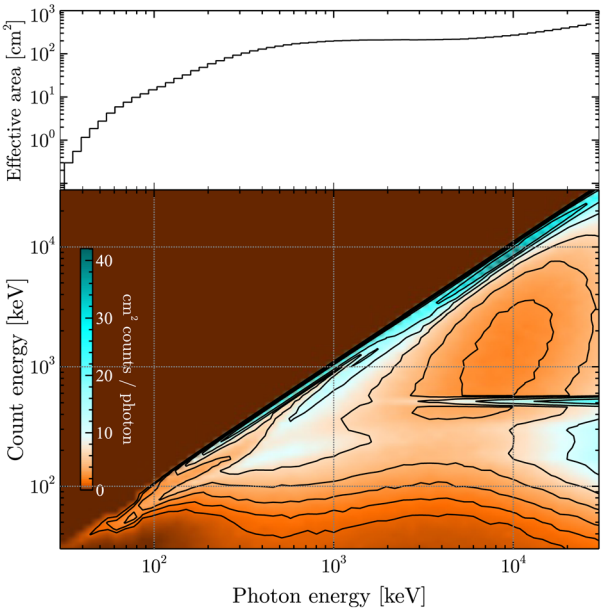

Figure B1. Simulated *RHESSI* response matrix of rear segments at 5° incidence (bottom panel). The response matrix has been used to generate the fit to the count energy spectrum (Fig. 3) as to obtain an estimate of the incident photon flux. By integrating over the count energy dimension, we obtain the effective area of the detector versus incident photon energy (top panel).

APPENDIX C: INSTRUMENTAL FEATURE IN *RHESSI* DATA OF SGR 1806–20 GIANT FLARE

A remarkable feature can be seen in the *RHESSI* light curve at $t_f - t_0 \sim 3.465$ s (see Fig. C1), coinciding with the initial pulse of the pulsating tail of the GF. It is primarily concentrated in the front segments, lasts for $\Delta t_f \sim 0.435$ s, and comprises a number of spikes, ∼0.09 s apart. The background-subtracted[7] spectrum of the feature is plotted in Fig. C2. The spikes are primarily visible below ∼300 keV and in the range ∼2.6–3 MeV in the front segments.

Following discussion with experts on the *RHESSI* instrumentation (Smith and Hurford, private communications), it was determined that these spikes are most likely an instrumental feature caused by the motion of an attenuator that deployed in response to the high count rate. Its motion is induced by putting a current through a wire, which contracts when heated. The heating was initiated at ∼3.36 s and the attenuator registered in the 'in' position at ∼3.75 s. The prompt movement, or rather impact of the attenuator on the stop, can produce microphonic noise in the detectors that may be recorded as an event; generally dominant in the front segments and varying significantly between the individual segments. The separate spikes may be explained by the fact that the attenuator bounced several times after the initial impact before it came to rest – each strike generating a burst of microphonics. At the time of writing this effect is not one of the possible sources of light-curve artefacts described on the *RHESSI* artefact web page.[8]

This instrumental feature must be taken into account when performing spectral or temporal analysis of the GF in the moments following the initial hard spike in the period $t - t_0 = 3$–4 s. The

[7] The background spectrum consists of a spectrum integrated over Δt_f taken just before the appearance of the instrumental feature at $t_f - t_0$.

[8] *RHESSI* artefact web page: http://hesperia.gsfc.nasa.gov/ssw/hessi/doc/guides/lightcurve_artifacts.htm.

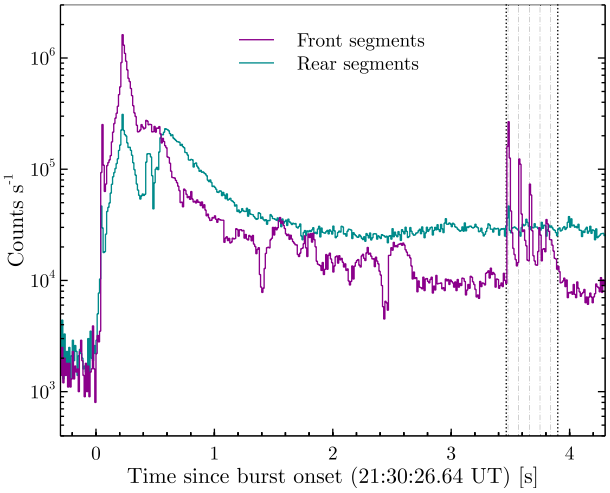

Figure C1. *RHESSI* count rate versus time in the front and rear segments of the detectors. The instrumental feature is apparent at $t - t_0 \sim 3.465$ s. The dotted lines denote the time-integration interval taken to generate the spectrum (see Fig. C2). The dash–dotted lines roughly indicate the individual peaks and are separated by ∼0.09 s. Note that the feature is primarily concentrated to the front segments.

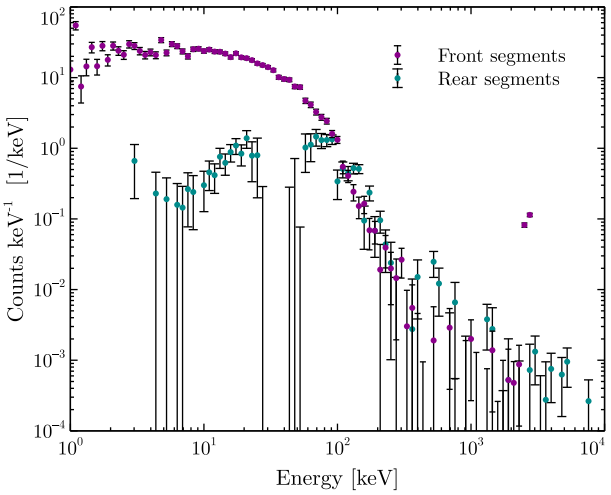

Figure C2. *RHESSI* (background-subtracted) spectral energy distribution of the instrumental feature. The magenta (cyan) dots denote the data recorded in the front (rear) segments. Note the presence of a high-energy peak at ∼2.5–3 MeV in the front segments.

RHESSI high-energy light curve (Fig. 2) and spectrum (Fig. 3) in this manuscript are composed of data recorded solely in the rear segments, where the presence of the instrumental feature is marginal. Moreover, the behaviour of the pulsating tail as a function of energy, as discussed in Section 2.3, is studied in the time range $t - t_0 = 5$–95 s, after this instrumental feature has subsided.

This paper has been typeset from a TEX/LATEX file prepared by the author.